2020

REMOTE SENSING OF PHYTOPLANKTON SIZE CLASSES ON THE NORTHEAST U.S. CONTINENTAL SHELF

Kyle J. Turner

University of Rhode Island, kjturner@uri.edu

REMOTE SENSING OF PHYTOPLANKTON SIZE CLASSES ON THE

NORTHEAST U.S. CONTINENTAL SHELF

BY

KYLE J. TURNER

A THESIS SUBMITTED IN PARTIAL FULFILLMENT OF THE REQUIREMENTS

FOR THE DEGREE OF MASTER OF SCIENCE

IN

OCEANOGRAPHY

UNIVERSITY OF RHODE ISLAND

2020

MASTER OF SCIENCE THESIS

OF

KYLE J. TURNER

APPROVED:

Thesis Committee:

Major Professor   Colleen Mouw

                      James Yoder

                      Yeqiao Wang

                      Kimberly Hyde

                      Brenton DeBoef
                      DEAN OF THE GRADUATE SCHOOL

UNIVERSITY OF RHODE ISLAND

2020

ABSTRACT

The size structure of phytoplankton communities influences important ecological and biogeochemical processes, including the transfer of energy through marine food webs. A variety of algorithms have been developed to estimate phytoplankton size classes (PSCs) from satellite ocean color data. However, many of these algorithms were developed for application to the open ocean, and their performance in more productive, optically complex continental shelf systems has not been fully evaluated. In this study, several existing PSC algorithms were applied in the Northeast U.S. continental shelf (NES) and assessed by comparison to *in situ* PSC estimates derived from a regional HPLC pigment data set. The effect of regional re-parameterization and incorporation of sea surface temperature (*SST*) into existing abundance-based model frameworks was investigated, and the models were validated using an independent data set of *in situ* and satellite match-ups. Abundance-based model re-parameterization alone did not result in significant improvement in performance in the NES compared with other models, however, the inclusion of *SST* led to a consistent reduction in model error for all size classes. Of two absorption-based algorithms tested, the best validating approach displayed similar performance metrics to the regional abundance-based model that included *SST*. The *SST*-dependent model was applied to monthly imagery composites of the NES region for April and September 2019, and qualitatively compared with imagery from the absorption-based approach. The results indicate the benefit of considering *SST* in abundance-based models and the applicability of absorption-based approaches in optically dynamic regions.

ACKNOWLEDGEMENTS

PREFACE

This thesis manuscript has been formatted to meet the criteria set by the Graduate School of the University of Rhode Island.

Table of Contents   **Page Number**

values obtained by performing a running bootstrap fit of the model (Eqs. 9 and 10) to the *in situ* parameterization data set ($N = 418$) sorted by increasing *SST*. The *SST*-parameter relationships were smoothed using a 5-point running average. Dashed lines indicate the *SST*-independent model (i.e., B-NES) parameters obtained when fitting the model to the full parameterization data

Figure 5. Satellite-derived $a_{ph}^*(\lambda)$ at 443, 490, 510, and 555 nm from the validation data set ($N = 368$; open circles) compared with the *in situ* $a_{ph}^*(\lambda)$ spectra ($N = 214$; gray lines) and the micro- and picoplankton basis spectra from the model of Ciotti

Figure 6. Bivariate histograms showing the satellite-to-*in situ* comparisons of [*Chl-a*], $a_{ph}(\lambda)$, and $a_{dg}(\lambda)$, shaded by number of observations: (a) [*Chl-a*] from the standard OC-CCI algorithm, (b) [*Chl-a*] from the regional algorithm of Pan et al. (2010), (c) $a_{ph}(443)$, (d) $a_{ph}(490)$, (e) $a_{ph}(510)$, (f) $a_{dg}(443)$, (g) $a_{dg}(490)$, and (h) $a_{dg}(510)$ from the standard OC-CCI algorithm (QAA_v5). The solid black line is the 1:1 line, dashed black lines indicate the 1:1 line $\pm 30\%$, and the red line is the Type-II regression line. N denotes the number of match-ups, *MAE* denotes the mean absolute error, δ denotes the bias, r denotes the correlation coefficient, and S denotes the regression slope. The $a_{ph}(\lambda)$ and $a_{dg}(\lambda)$ data are shown using the same

PUBLICATION STATUS

This manuscript is being prepared for submission to the journal *Frontiers in Remote Sensing.*

1.   INTRODUCTION

Phytoplankton form the base of pelagic food webs and are a key component of biogeochemical cycles that impact global climate (i.e., carbon cycle) (Longhurst et al., 1995; Field et al., 1998; Behrenfeld et al., 2006). Phytoplankton in the ocean are taxonomically diverse, spanning nine orders of magnitude in cell volume and exhibiting an array of unique morphological and physiological characteristics (Finkel et al., 2010; Caron et al., 2012). Phytoplankton community composition and biomass are highly variable in time and space, changing in response to both bottom-up (i.e., nutrient availability, environmental conditions) and top-down (i.e., grazing) controls. Understanding the dynamics of phytoplankton in terms of both abundance and community structure is critical to better understanding their role in marine ecology and biogeochemistry.

Functional traits or classes have been applied as an effective means of studying phytoplankton community dynamics, while reducing the requirement for detailed taxonomic discrimination (IOCCG, 2014; Nair et al., 2008; Le Quéré et al., 2005). Phytoplankton cell size is considered a fundamental trait as it affects many important biological and ecological processes, including photosynthesis (Uitz et al., 2008), nutrient uptake (Raven, 1998), growth rate (Marañón, 2015), light absorption (Ciotti et al., 2002; Bricaud, 2004), carbon export (Guidi et al., 2009; Mouw et al., 2016), and the transfer of energy through food webs (Boyce et al., 2015). Thus, the size structure of phytoplankton assemblages can serve as a valuable indicator of the state of marine ecosystems and their response to

2

environmental changes (i.e., ocean warming) (Platt and Sathyendranath, 2008; Marinov et al., 2010; Morán et al., 2010). Following the classification of Sieburth et al. (1978), phytoplankton are conventionally partitioned into three phytoplankton size classes (PSCs): picoplankton (0.2-2 μm), nanoplankton (2-20 μm), and microplankton (20-200 μm).

A number of methods exist for quantifying PSCs *in situ*, including microscopy, size-fractionated filtration (SFF), conventional and imaging flow cytometry (Olson and Sosik, 2007), and high-performance liquid chromatography (HPLC) marker pigments, each with advantages and limitations (IOCCG, 2014). While these methods have proven accurate and useful, they are labor-intensive, time-consuming, and expensive. As a result, the availability of *in situ* PSC data remains quite sparse in space and time, thus limiting their utility in studying and modeling large scale, dynamic ocean and ecosystem processes. Satellite remote sensing, capable of providing regularly repeated, synoptic coverage of upper ocean optical properties, provides a means to characterize PSCs at spatial and temporal resolutions unattainable with *in situ* sampling techniques. Given this fact, deriving information on PSCs from satellite ocean color data is an active area of research, and a variety of algorithms have been developed for both global ocean (Brewin et al., 2015; Hirata et al., 2011) and regional application (Brito et al., 2015; Di Cicco et al., 2017; Gittings et al., 2019; Lamont et al., 2018; Sun et al., 2019, 2018). Most current approaches for detecting PSCs from remote sensing can be categorized as either "abundance-based" or "absorption-based" (IOCCG, 2014;

3

Mouw et al., 2017b). These approaches differ in terms of their theoretical frameworks and the remotely sensed parameters utilized as inputs.

Abundance-based algorithms exploit the generally observed co-variance of phytoplankton size structure and total biomass [indexed by its proxy, chlorophyll-a concentration ([*Chl-a*])] to estimate dominance or relative biomass fractions of PSCs (Uitz et al., 2006; Brewin et al., 2010; Hirata et al., 2011). For example, it is well established that picoplankton, such as the cyanobacteria *Prochlorococcus* and *Synechococcus*, dominate in low-nutrient, oligotrophic environments (i.e., open ocean gyres) and larger-celled microplankton, such as diatoms, comprise a greater fraction of total biomass in eutrophic, nutrient-rich regions (i.e., upwelling zones) (Margalef, 1978; Chisholm et al., 1988; Yentsch and Phinney, 1989). Abundance-based methods rely on empirical or semi-empirical relationships based on coincident *in situ* observations of size fractionated biomass (i.e., from HPLC marker pigments or SFF) and [*Chl-a*] to estimate PSCs as a function of [*Chl-a*]. Given that [*Chl-a*] is perhaps the most widely used and well-validated satellite ocean color product, abundance-based methods offer a straightforward, "user-friendly" approach for estimating PSCs from remote sensing. Yet, these methods are only an indirect approximation of PSCs, and the empirical relationships they are based on are subject to change over time, requiring ongoing assessment and re-calibration (Mouw et al., 2017b). Recent studies have demonstrated that the incorporation of additional environmental information attainable from remote sensing (i.e. sea surface temperature [*SST*]) can improve the retrieval accuracy of

4

abundance-based models (Ward, 2015; Brewin et al., 2017; Moore and Brown, 2020).

Absorption-based algorithms distinguish PSCs directly from spectral variations in phytoplankton absorption [$a_{ph}(\lambda)$], the amount of light absorbed by phytoplankton across the visible spectrum, which influences, and can be inversely derived from, the reflectance signal measured by a satellite ocean color sensor [remote sensing reflectance; $R_{rs}(\lambda)$] (Ciotti et al., 2002; Ciotti and Bricaud, 2006; Devred et al., 2011, 2006; Mouw and Yoder, 2010). Smaller cells absorb visible light more efficiently than larger cells due to the way photosynthetic pigments are packaged within larger cells. This "package effect" results in a flattening of the chlorophyll-normalized absorption spectrum [$a_{ph}^*(\lambda)$] with increasing cell size, with the most pronounced change at blue wavelengths (i.e., around 440 nm) (Morel and Bricaud, 1981; Morel, 1987; Bricaud et al., 1988). Ciotti et al. (2002) demonstrated that despite physiological and taxonomic variability, cell size could explain >80% of the variance in the spectral shape of $a_{ph}^*(\lambda)$ over the wavelength range 400-700 nm. An advantage of absorption-based methods over abundance-based approaches is that they are able to detect changes in PSCs that do not co-vary with [*Chl-a*] (i.e., blooms of different sized cells may comprise the same [*Chl-a*]). Moreover, as absorption-based methods are based on direct optical responses rather than indirect empirical relationships, they are less likely to require re-calibration over time or for different ocean regions. However, the limited spectral resolution of current multi-spectral ocean color sensors can make retrieving

accurate $a_{ph}(\lambda)$ spectral shape challenging, particularly in optically complex coastal and continental shelf waters with high concentrations of colored dissolved organic matter (CDOM) and non-algal particles (NAP), which overlap with phytoplankton in their contribution to the total light absorption in the blue region of the spectra.

Given the unique strengths and limitations of these different approaches to detecting PSCs from remote sensing, evaluating how they perform in different ocean regions, and whether they may be optimized for regional application, is essential. A number of studies have successfully retrieved PSCs at regional scales (i.e., shelf seas), including the Red Sea (Gittings et al., 2019), the Mediterranean Sea (Di Cicco et al., 2017), the Bohai and Yellow Seas (Sun et al., 2018, 2019), the Western Iberian coast (Brito et al., 2015), and the southern coast of Africa (Lamont et al., 2018), through re-parameterization of global abundance-based models with local *in situ* data sets. These studies demonstrate the potential benefit of PSC model optimization for regional applications, including regional-scale food-web modeling and ecosystem-based fisheries management.

The northeast U.S. continental shelf (denoted NES throughout the remainder of the text), is a highly productive, temperate marine ecosystem that supports many commercially and recreationally important fisheries (Hare et al., 2016; National Marine Fisheries Service, 2018). The NES region is physically dynamic and optically complex (Pan et al., 2008; Mannino et al., 2014), thus necessitating evaluation and potential optimization of existing global PSC algorithms to ensure their accuracy. Phytoplankton species composition and

6

abundance in the NES varies seasonally, with diatoms dominating in a typical winter-spring bloom, and other taxa, such as dinoflagellates, cryptophytes, and cyanobacteria, becoming more prevalent during the summer (O'Reilly and Zetlin, 1998; Pan et al., 2011; Richaud et al., 2016).

The aim of this study is to evaluate and optimize several existing abundance-based and absorption-based PSC algorithms for application to ocean color imagery in the NES region, with the goal of improving PSC imagery products for long-term time series investigations and integration into regional ecosystem and fisheries modeling efforts. Specifically, the following scientific questions are addressed:

- To what extent does regional re-parameterization using a local *in situ* data set improve the performance of abundance-based PSC algorithms in the NES?

- Does the incorporation of *SST* into abundance-based models improve accuracy for predicting PSCs in the NES?

- How do abundance-based and absorption-based models compare in their estimation of PSCs in the NES?

- What spatial and temporal patterns of phytoplankton size structure are observed in the NES?

Table 1. Symbols and definitions.

Symbol	Definition	Units (if applicable)
$a_d(\lambda)$	absorption coefficient of non-algal particles	m^{-1}
$a_{dg}(\lambda)$	absorption coefficient of colored dissolved organic matter + non-algal particles	m^{-1}
$a_g(\lambda)$	absorption coefficient of colored dissolved organic matter	m^{-1}
[*Allo*]	alloxanthin concentration	mg m^{-3}
$a_{ph}(\lambda)$	absorption coefficient of phytoplankton	m^{-1}
$a_{ph}^*(\lambda)$	chlorophyll-specific absorption coefficient of phytoplankton	m^2 mg^{-1}
[*But-fuco*]	19'-butanoyloxyfucoxanthin concentration	mg m^{-3}
[*Chl-a*]	chlorophyll-a concentration	mg m^{-3}
C_{DP}	chlorophyll-a concentration reconstructed from the weighted sum of diagnostic pigments	mg m^{-3}
C_{HPLC}	chlorophyll-a concentration measured by high-performance liquid chromatography	mg m^{-3}
C_{size}	chlorophyll-a concentration specific to size class "size"	mg m^{-3}
C^m_{size}	asymptotic maximum chlorophyll-a concentration of size class "size"	mg m^{-3}
D_{size}	fraction of size class "size" as total chlorophyll-a tends to zero	unitless
F_{size}	fraction of size class "size"	unitless
[*Fuco*]	fucoxanthin concentration	mg m^{-3}
GB	Georges Bank	-
GoM	Gulf of Maine	-
[*Hex-fuco*]	19'hexanoyloxyfucoxanthin concentration	mg m^{-3}
MAB	Middle Atlantic Bight	-
MAE	mean absolute error	unitless
NES	northeast U.S. continental shelf	-
[*Perid*]	peridinin concentration	mg m^{-3}
r	Pearson correlation coefficient	unitless
$R_{rs}(\lambda)$	remote sensing reflectance	sr^{-1}
S	slope of a Type-II linear regression	unitless
SST	sea surface temperature	ºC
SFF	size-fractionated filtration	-
[*TAcc*]	total concentration of accessory pigments	mg m^{-3}
[*TChl-b*]	total chlorophyll-b concentration	mg m^{-3}
[*Zea*]	zeaxanthin concentration	mg m^{-3}
δ	bias	unitless

2. DATA AND METHODS

2.1. Study Area

The NES region (35ºN-45.5ºN, 64ºW-77ºW) extends along the east coast of the U.S. from Cape Hatteras, NC to Nova Scotia (Fig. 1). The region includes three primary subregions: the Gulf of Maine (GoM), Georges Bank (GB), and the Mid-Atlantic Bight (MAB). The continental shelf is commonly delineated as inshore of the 200 m isobath, with deeper basins in the GoM (i.e., Georges Basin) that exceed 300 m depth. The NES is influenced by two major current systems: the warm, saline, northward flowing Gulf Stream, and the colder, fresher, southward flowing Labrador Current. Mesoscale features (i.e., eddies, fronts) and interannual variations in the path of the Gulf Stream and flow of the Labrador Current affect nutrient fluxes, productivity, and phytoplankton composition across the NES (Schollaert et al., 2004; Saba et al., 2015). The NES has experienced rapid warming (Pershing et al., 2015), which has been connected to changes in phytoplankton bloom dynamics (Hunter-Cevera et al., 2016), and the distributions of fish and other marine species (Kleisner et al., 2017). The NES has been extensively sampled relative to other parts of the global ocean, with routine hydrographic and biological surveys conducted throughout the region since the late 1970s (O'Reilly and Zetlin, 1998). At present, NOAA's Northeast Fisheries Science Center (NEFSC) conducts quarterly Ecosystem Monitoring (EcoMon) surveys, which provide a range of hydrographic and biological data for the region (National Marine Fisheries Service, 2020).

2.2. *In situ* Data

Discrete surface (upper 10 m) samples of HPLC pigments and the spectral absorption coefficients of phytoplankton [$a_{ph}(\lambda)$], CDOM [$a_g(\lambda)$], and NAP [$a_d(\lambda)$] collected throughout the NES region from 2003 to 2018 were acquired from NASA's SeaWiFS Bio-optical Archive and Storage System data repository (SeaBASS; https://seabass.gsfc.nasa.gov/) (Fig. 1). The compiled data were derived from several different cruises and experiments, with the largest portion from the Impacts of Climate Variability on Primary Production and Carbon Distributions in the Middle Atlantic Bight and Gulf of Maine (CliVEC) field campaign and the University of New Hampshire Western Gulf of Maine time series (Table 2). Only HPLC pigment samples containing a full set of seven diagnostic pigments required for estimating PSCs (i.e., fucoxanthin, peridinin, 19'-hexanoyloxyfucoxanthin, 19'-butanoyloxyfucoxanthin, alloxanthin, total chlorophyll-b, and zeaxanthin) were included in this analysis (see Section 2.6). For the absorption data, only measurements with a spectral resolution of 1-nm over the range of 400-700 nm with coincident HPLC pigments were retained. In order to calculate the combined absorption of CDOM and NAP [$a_{dg}(\lambda)$], a parameter routinely retrieved by satellite inversion algorithms, measurements of $a_g(\lambda)$ without matching $a_d(\lambda)$ (and vice-versa) were excluded. If a station had multiple samples within the upper 10 m, the data were averaged. To limit the effects of shallow water and near-shore processes, stations with a water column <25 m were removed prior to analysis.
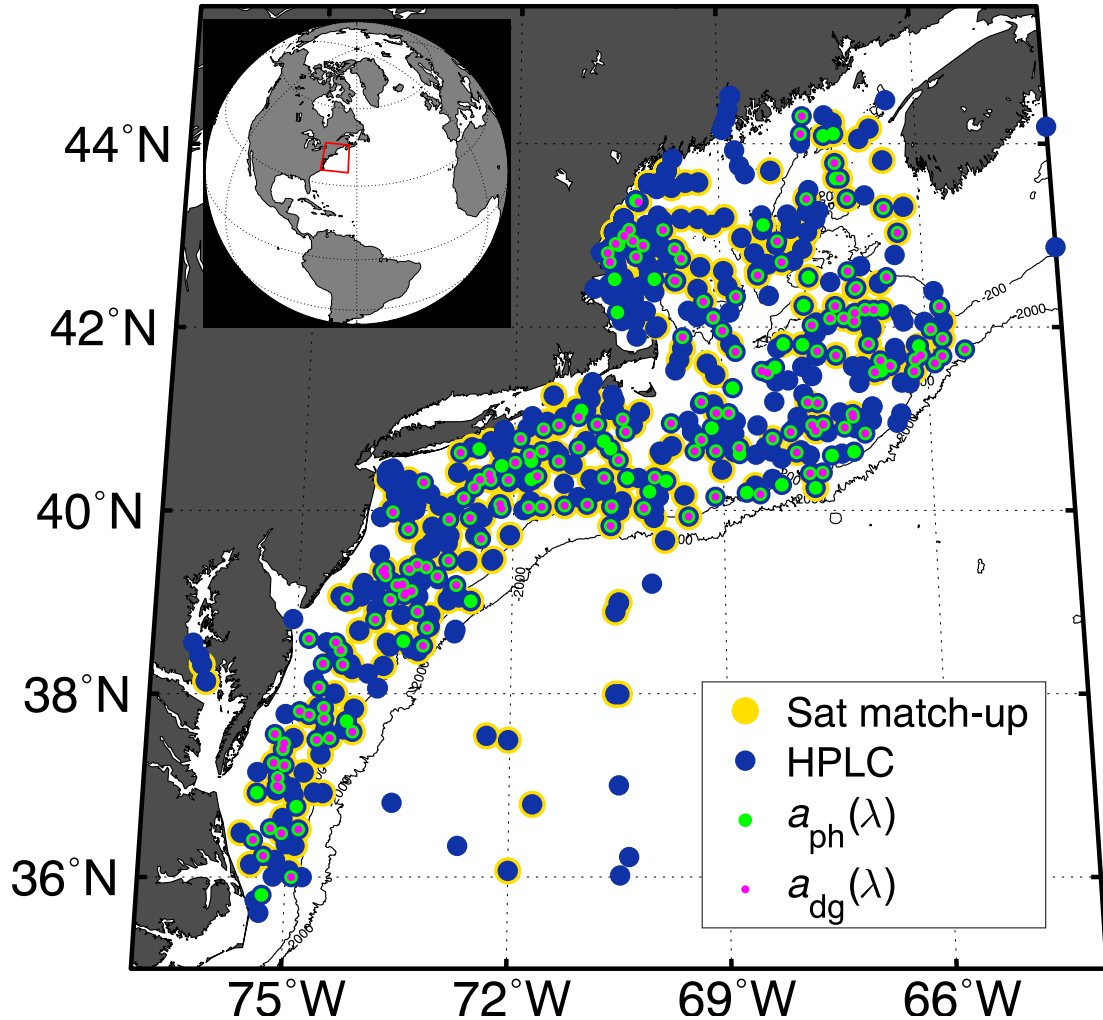
Figure 1. Locations of the *in situ* data and satellite match-ups used in this study. The 200 m and 2000 m isobaths from the 2019 General Bathymetric Chart of the Oceans (https://www.gebco.net/) are shown for reference. See Table 2 for information on data sources.

An additional 40 HPLC, 24 $a_{ph}(\lambda)$, and 14 $a_g(\lambda)/a_d(\lambda)$ samples collected on the Summer 2018 and Fall 2018 NOAA EcoMon surveys were added to the data from SeaBASS. HPLC pigment samples from these cruises were collected by filtering ~1-2 L of seawater onto 25 mm GF/F filters (0.7 μm pore size) which were subsequently frozen in liquid nitrogen and analyzed at Horn Point Laboratory (University of Maryland Center for Environmental Science). Absorption

measurements from the EcoMon surveys were collected and analyzed according to the NASA Ocean Optics Protocols (Mueller et al., 2003) following the procedures detailed in Mouw et al. (2017a).

Quality assurance (QA) for the HPLC pigment data was carried out following the procedure of Uitz et al. (2006). First, to account for differences in the detection limits and sensitivities of different HPLC processing methods, pigment concentrations <0.001 mg m^{-3} were set to zero. Then, utilizing the relationship of Trees et al. (2000), who demonstrated that [*Chl-a*] and the total concentration of major accessory pigments ([*TAcc*]) co-vary in log-linear fashion within the euphotic zone of diverse oceanic regions, a robust linear regression analysis (MATLAB function *robustfit.m*) of [*TAcc*] on [*Chl-a*] was performed to identify outliers. Any points exceeding three standard deviations with respect to the mean of the residuals (data – regression) were excluded. QA for the $a_{ph}(\lambda)$, $a_g(\lambda)$, and $a_d(\lambda)$ data consisted of the following steps: (1) overly noisy spectra were manually identified and removed; (2) spectra with negative values (not exceeding -0.1) were offset by the most negative value (Grunert et al., 2019); (3) spectra were smoothed using a Savitsky-Golay filtering technique (MATLAB function *sgolayfilt.m*) with a 9-nm smoothing window (Torrecilla et al., 2011). The $a_g(\lambda)$ and $a_d(\lambda)$ values were then summed to obtain $a_{dg}(\lambda)$. After QA, a total of 786 HPLC, 214 $a_{ph}(\lambda)$, and 173 $a_{dg}(\lambda)$ measurements remained. The pigment data were representative of every month of the year, with a slight bias towards summer months, whereas $a_{ph}(\lambda)$ and $a_{dg}(\lambda)$ data were almost exclusively limited to summer and fall months (Fig. 2).

Table 2. Summary of *in situ* data sources. *N* denotes the number of samples (after QA), where the number in parentheses refers to the number of satellite match-ups. Citations for the individual data sets from SeaBASS are also provided.

Cruise/Experiment – P.I.(s)	Year(s)	Month(s)	N, HPLC	N, $a_{ph}(\lambda)$	N, $a_{dg}(\lambda)$
Impacts of Climate Variability on Primary Production and Carbon Distributions in the Middle Atlantic Bight and Gulf of Maine (CliVEC) – Mannino et al., 2009	2009-2012	Feb, May, Jun, Aug, Nov	424 (212)	182 (101)	153 (86)
NOAA Ecosystem Monitoring (EcoMon) – Mannino et al., 2013	2013, 2018	Feb, Aug, Nov	71 (41)	24 (18)	14 (9)
Optical and Nutrient Dependence of Quantum Efficiency (OnDeque3) – Marra et al., 2008	2008	Jul	26 (15)	0	0
Tara Oceans Expedition – Boss et al., 2009	2012	Jan, Feb	2	0	0
East Coast Ocean Acidification (ECOA-1) – Mannino et al., 2015	2015	Jun, Jul	37 (16)	0	0
LOBO timeseries – Roesler, 2009	2009	Mar	6	0	0
Western Gulf of Maine – Moore, 2006	2006-2009	All months	188 (68)	3	0
Ocean Color Cal Val (OCV) – Hooker et al., 2005	2007, 2009	May, Nov	16 (7)	0	0
COASTAL (C7) – Hooker, 2000	2008	Oct	6 (5)	5 (4)	6 (4)
Delaware and Chesapeake Bay Fluorescence – Chekalyuk, 2008	2008	May	1	0	0
2009oct_Chesapeake – Gould, 2009	2009	Oct	7 (3)	0	0
BIOCOMPLEXITY – Harding, 2001	2003	Aug	2 (1)	0	0
		Totals:	786 (368)	214 (123)	173 (99)
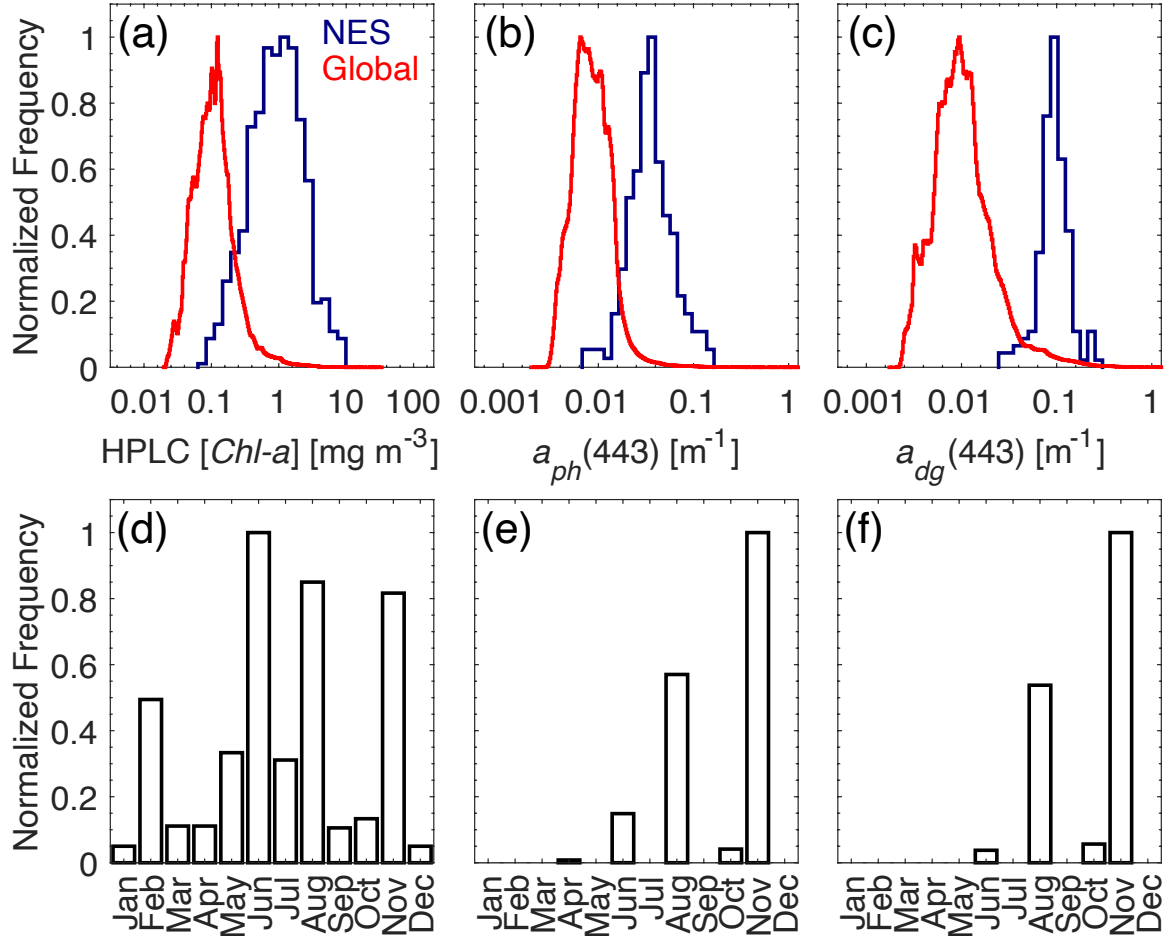
Figure 2. Relative frequencies of *in situ* observations from the NES data set used in this study (blue stairs): (a) HPLC-measured [*Chl-a*] ($N = 786$), (b) $a_{ph}(443)$ ($N = 214$) and (c) $a_{dg}(443)$ ($N = 173$), with their respective monthly distributions (d-f, black bars). Global distributions from an OC-CCI v4.2 annual satellite composite for 2018 are overlain for comparison (red line). Frequencies were normalized by the maximum value. OC-CCI v4.2 data were downloaded from https://esa-oceancolour-cci.org/.

2.3. Satellite Data

Daily, Level-3 mapped (4-km resolution, sinusoidally projected) estimates of $R_{rs}(\lambda)$, [*Chl-a*], $a_{ph}(\lambda)$, and $a_{dg}(\lambda)$ from the most recent version (4.2) of the European Space Agency's (ESA) Ocean Colour – Climate Change Initiative product (OC-CCI v4.2; Sathyendranath et al., 2019) at the time of the initiation of

this study were downloaded from https://esa-oceancolour-cci.org/. These parameters are required inputs for the PSC algorithms evaluated in this study (see Section 2.7). OC-CCI v4.2 consists of globally merged, bias-corrected data from the Sea-viewing Wide-Field-of-View Sensor (SeaWiFS), Medium Resolution Imaging Spectrometer (MERIS), Moderate Resolution Imaging Spectroradiometer (MODIS-Aqua), and Visible Infrared Imaging Radiometer Suite (VIIRS-SNPP) satellite sensors over the period 1997-2019. The multi-sensor data are band-shifted to standard SeaWiFS wavelengths (412, 443, 490, 510, 555, and 670 nm) and include per-pixel uncertainty estimates. OC-CCI v4.2 also incorporates the latest NASA reprocessing (R2018), which corrected for drift in the MODIS-Aqua sensor. The reader is referred to the OC-CCI v4.2 Product User Guide (https://esa-oceancolour-cci.org/documents-list) for a more detailed overview.

The standard OC-CCI [*Chl-a*] algorithm uses a blended combination of NASA's OC3, OCI, and OC5 algorithms (O'Reilly et al., 1998; Gohin et al., 2002; Hu et al., 2012) based on optical water classes (Moore et al., 2009; Jackson et al., 2017), which improves performance in optically complex waters. In addition to the standard algorithm, [*Chl-a*] was also calculated using the regional algorithm of Pan et al. (2010). This regional empirical algorithm was developed based on coincident *in situ* measurements of HPLC pigments and $R_{rs}(\lambda)$ collected at various locations across the MAB and GoM. The algorithm was applied using the published coefficients for SeaWiFS wavebands. The standard OC-CCI $a_{ph}(\lambda)$ and $a_{dg}(\lambda)$

products are derived using the Quasi-Analytical Algorithm (QAA_v5) of Lee et al. (2009).

For validation of the satellite input products ([*Chl-a*], $a_{ph}(\lambda)$, and $a_{dg}(\lambda)$) and PSC algorithm estimates, *in situ* samples were matched in time and space with the satellite data. Following standard methods, match-ups were determined as the median of a 3x3 pixel box centered on the sampling location (nearest latitude and longitude), where only match-ups with at least 5 valid pixels and a median coefficient of variation of <0.15 for $R_{rs}(\lambda)$ bands between 412 and 555 nm were used to ensure spatial homogeneity (Bailey and Werdell, 2006). Given that OC-CCI is a daily, multi-sensor product, a same-day coincidence window was used rather than the more stringent ±3-hour window recommended for a single mission by Bailey and Werdell (2006). This resulted in 368 [*Chl-a*], 123 $a_{ph}(\lambda)$, and 99 $a_{dg}(\lambda)$ match-ups (Table 2).

Recent studies (Brewin et al., 2017, Moore and Brown, 2020) have demonstrated that the inclusion of *SST* can improve the performance of abundance-based algorithms. To explore the relationship between *SST* and the parameters of the Brewin et al. (2010) three-component PSC model (see Section 2.7), all *in situ* pigment samples were matched with daily estimates of *SST* from the Multi-scale Ultra-high Resolution *SST* analysis (MUR version 4.1) (Chin et al., 2017). MUR is a gap-filled, 1-km resolution gridded global *SST* product that fuses night-time infra-red *SST* retrievals from the MODIS sensor with multiple other in-orbit infra-red/microwave instruments and data from NOAA's *in situ SST* Quality

Monitor (iQuam) database (Xu and Ignatov, 2014). Data for the period June 1, 2002 – December 31, 2019 were downloaded freely from NASA's Physical Oceanography Distributed Active Archive Center (https://podaac.jpl.nasa.gov).

2.4. Partitioning of Data for Model Re-parameterization and Validation

To allow for both the re-parameterization of abundance-based PSC models (see Sections 2.7.1.6 and 2.7.1.7) and independent model validation, the HPLC pigment data were split into two separate data sets. Of the 786 total samples, the 368 samples with a satellite [*Chl-a*] match-up (~47% of the data) were removed and reserved for independent validation and are referred to as the validation data set. The remainder of the *in situ* pigment data ($N = 418$) were used for model re-parameterization, and are referred to as the parameterization data set.

2.5. Statistical Performance Metrics

Several statistical metrics were used to compare algorithm estimates with the *in situ* data and evaluate performance. As a measure of accuracy, the mean absolute error (*MAE*) was used. While many studies commonly use root mean square error (*RMSE*), *MAE* has been recommended as a more unambiguous and appropriate metric for model assessment (Willmott and Matsuura, 2005; Seegers et al., 2018). As a measure of systematic bias, the mean bias (δ) was used. The *MAE* and δ are calculated according to:

$$MAE = \frac{1}{N} \sum_{i=1}^{N} |M_i - O_i| \tag{1}$$

and

$$\delta = \frac{1}{N} \sum_{i=1}^{N} (M_i - O_i), \qquad (2)$$

where *M*, *O*, and *N* represent the modeled value (e.g., satellite estimate), the observed value (*in situ*), and the number of observations, respectively. A positive (negative) δ indicates a model's tendency to systematically overestimate (underestimate) the variable of interest. The Pearson correlation coefficient (*r*) and slope of a Type-II linear regression (*S*) were also computed for additional comparison between modeled and *in situ* values (Brewin et al., 2015b; Werdell et al., 2013). Type-II regression (MATLAB function *lsqfitgm.m*) was applied rather than Type-I regression as it accounts for the inherent measurement uncertainties of *in situ* field data (Laws and Archie, 1981). While values of *r* and *S* that are close to one generally indicate better agreement between model estimates and *in situ* observations, *r* and *S* alone provide no information on the accuracy or bias of a given model, and thus are viewed secondarily to the *MAE* and δ when assessing model performance. Statistical calculations involving total or size-specific [*Chl-a*], $a_{ph}(\lambda)$, or $a_{dg}(\lambda)$ were performed in $\log_{10}$ space, while calculations involving size fractions were performed in linear space.

2.6.   Estimation of PSCs from HPLC Pigments

For algorithm re-parameterization and validation, PSCs were estimated from the HPLC pigment data following the Diagnostic Pigment Analysis (DPA) method (Brewin et al., 2010; Brewin et al., 2015a; Claustre, 2005; Devred et al., 2011; Uitz et al., 2006; Vidussi et al., 2001). This method has been extensively

used for the development and validation of satellite PSC algorithms, given the relative abundance of HPLC pigment data compared with SFF and other *in situ* methods*.* The DPA approach involves first reconstructing the measured [*Chl-a*] (denoted here as C_{HPLC}) from the weighted sum of seven diagnostic phytoplankton pigments (denoted C_{DP}) according to:

$$C_{DP} = \sum_{i=1}^{7} W_i P_i, \tag{3}$$

where [*W*] represents pigment-specific weighting coefficients and [*P*] is the set of seven diagnostic pigments: {fucoxanthin ([*Fuco*]), peridinin ([*Perid*]), 19'-hexanoyloxyfucoxanthin ([*Hex-fuco*]), 19'-butanoyloxyfucoxanthin ([*But-fuco*]), alloxanthin ([*Allo*]), total chlorophyll-b ([*TChl-b*]), zeaxanthin ([*Zea*])}. To derive an optimal set of weighting coefficients from the NES pigment data set, a multi-linear regression of [*P*] on C_{HPLC} was performed. The newly computed weighting coefficients compared reasonably with those obtained from previous studies (Table 3), with the exception of large differences observed for the weights attributed to [*But-fuco*] and [*Allo*], which may be due to differences in community composition in the NES compared with the global ocean. The new weights yielded close agreement between C_{DP} and C_{HPLC} (*MAE* = 0.12, *r* = 0.98), and demonstrated better results relative to using the unweighted sum of the diagnostic pigments (Vidussi et al., 2001), or the commonly applied weighting coefficients of Uitz et al. (2006), which were derived from a large global pigment database (Fig. 3, Table 3).

The fractional contributions of micro-, nano-, and picoplankton were estimated from the ratios of the diagnostic pigments attributed to each size class to C_{DP}. Two diagnostic pigments were attributed to microplankton: [*Fuco*] and [*Perid*], associated with diatoms and dinoflagellates, respectively. Acknowledging
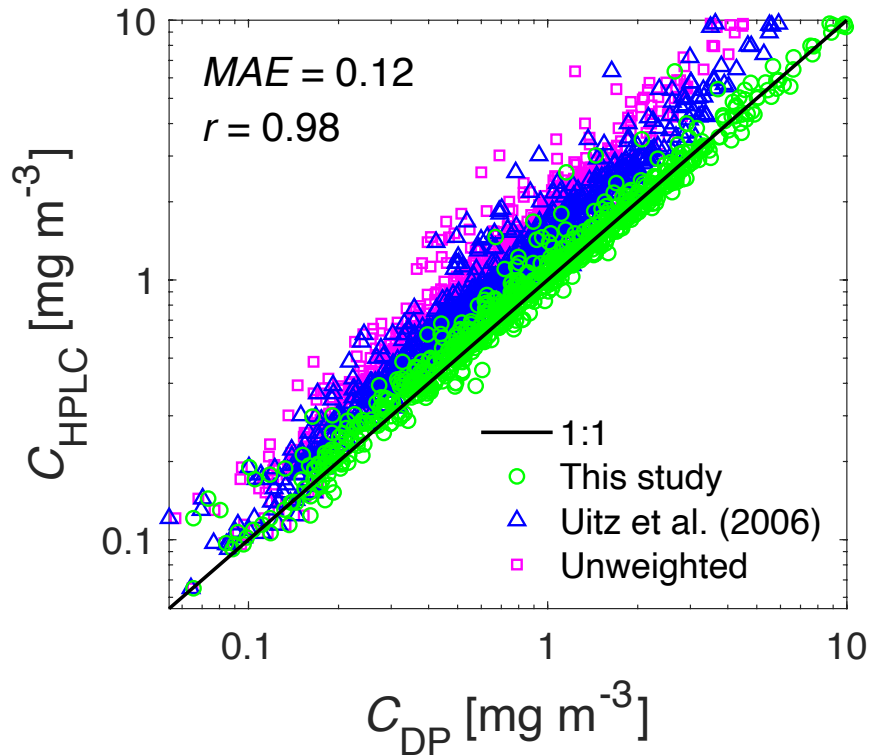
Figure 3. Comparison of the HPLC-measured [*Chl-a*] (C_{HPLC}) and the [*Chl-a*] reconstructed from the sum of seven diagnostic pigments (C_{DP}) using the weighting coefficients derived from this study (green circles; $MAE = 0.12$, $r = 0.98$), the weights derived by Uitz et al. (2006) from a global data set (blue triangles; $MAE = 0.47$, $r = 0.96$), and no weighting coefficients (magenta squares; $MAE = 0.62$, $r = 0.96$).

that [*Fuco*] is also present in prymnesiophytes and chrysophytes, and that diatoms can also occupy the nano size range, Devred et al. (2011) introduced a

modification that attributes a portion of [*Fuco*] (P_1) to nanoplankton, such that $P_1 = P_{1,nano} + P_{1,micro}$. In their approach, $P_{1,nano}$ is estimated from the equation:

$$P_{1,nano} = 10^{[q_1 log_{10}(P_3) + q_2 log_{10}(P_4)]}, \qquad (4)$$

where P_3 and P_4 are the pigments [*Hex-fuco*] and [*But-fuco*], respectively, and q_1 and q_2 are the coefficients of a 1% multi-linear quantile regression of P_1 on P_3 and P_4. Following the same approach, The coefficients q_1 and q_2 were re-computed for the NES pigment dataset, obtaining values of $q_1 = 0.999$ and $q_2 = 0.271$, and $P_{1,nano}$ was estimated using Eq. (4). In any instance where the estimated $P_{1,nano}$ was found to be greater than P_1, it was set equal to P_1. The fraction of microplankton (F_{micro}) was then calculated according to:

$$F_{micro} = \frac{\sum_{i=1}^{2} W_i P_i - W_1 P_{1,nano}}{C_{DP}}. \qquad (5)$$

Three diagnostic pigments were used to estimate nanoplankton: [*Hex-fuco*], [*But-fuco*], and [*Allo*], attributed to prymnesiophytes, pelagophytes, and cryptophytes, respectively (Brewin et al., 2015a; Roy, 2011; Uitz et al., 2006). Brewin et al. (2010) proposed an adjustment that attributes a portion of [*Hex-fuco*] to picoeukaryotes (picoplankton) in ultra-oligotrophic environments ([*Chl-a*] < 0.08 mg m^{-3}). However, considering that only one sample in the data set used in this study met this criterion ([*Chl-a*] = 0.07 mg m^{-3}) and the adjustment was found to make only minor difference (not shown), it was excluded for simplicity. Incorporating the [*Fuco*] modification of Devred et al. (2011), the fraction of nanoplankton (F_{nano}) was calculated as:

$$F_{nano} = \frac{\sum_{i=3}^{5} W_i P_i + W_1 P_{1,nano}}{C_{DP}}. \tag{6}$$

The final two diagnostic pigments: [*TChl-b*] and [*Zea*], were attributed to the picoplankton class, the former associated with prochlorophytes and chlorophytes and the latter with prochlorophytes and cyanobacteria (Chisholm et al., 1988; Uitz et al., 2006; Roy, 2011). The fraction of picoplankton (F_{pico}) was computed as:

$$F_{pico} = \frac{\sum_{i=6}^{7} W_i P_i}{C_{DP}}. \tag{7}$$

Table 3. Diagnostic pigments [*P*] and their associated taxonomic groups and attributed size classes, along with weighting coefficients [*W*] obtained from this study and previous studies. The number of data points and geographical regions of each study are also provided.

Pigment [*P*]	Primary taxonomic group(s)	Attributed size class(es)	Weights [*W*]			
			This study	*Uitz et al. (2006)*	*Brewin et al. (2015a)*	*Brewin et al. (2017)*
Fucoxanthin (P_1)	Diatoms	Micro/ nano	2.20	1.41	1.51	1.65
Peridinin (P_2)	Dinoflagellates	Micro	1.08	1.41	1.35	1.04
19'-Hex (P_3)	Prymnesiophytes	Nano	0.86	1.27	0.95	0.78
19'-But (P_4)	Pelagophytes	Nano	3.63	0.35	0.85	1.19
Alloxanthin (P_5)	Cryptophytes	Nano	-0.10	0.6	2.71	3.14
Total chlorophyll-b (P_6)	Prochlorophytes, Chlorophytes	Pico	1.21	1.01	1.27	1.38
Zeaxanthin (P_7)	Prochlorophytes, Cyanobacteria	Pico	0.99	0.86	0.93	1.02
		Number of data points	786	2419	5841	2239
		Geographic region	NES	Global	Global	North Atlantic

Once F_{micro}, F_{nano}, and F_{pico} (collectively referred to as F_{size}) were determined, the [*Chl-a*] specific to each size class (collectively referred to as C_{size}) was calculated by multiplying F_{size} by C_{HPLC}, such that:

$$C_{micro} = F_{micro}C_{HPLC}, \tag{8a}$$

$$C_{nano} = F_{nano}C_{HPLC}, \tag{8b}$$

$$C_{pico} = F_{pico}C_{HPLC}. \tag{8c}$$

2.7. PSC Algorithms

A variety of PSC algorithms, including purely abundance-based methods, abundance-based methods that include *SST*, and absorption-based approaches, were selected for optimization and/or evaluation in this study. The abundance-based models chosen are among the most commonly applied in the literature, and have been successfully re-parameterized for studies in diverse ocean regions, including continental shelf systems (Brito et al., 2015; Sun et al., 2018). The absorption-based models were chosen based on their global performance metrics (Mouw et al., 2017b), and consistency with phytoplankton phenology metrics (Kostadinov et al., 2017). The following sections provide brief overviews of each model, including their principal frameworks, methods used for model development/parameterization, and key differences. For more comprehensive information, the reader is referred to the original publications and the reviews of Mouw et al. (2017b) and IOCCG (2014).

2.7.1. Abundance-Based

2.7.1.1. Brewin et al. (2010, 2015a)

The three-component model of Brewin et al. (2010) relates the fractional contribution of combined pico- and nanoplankton ($F_{pico,nano}$) and picoplankton (F_{pico}) to [Chl-a] using two exponential functions (Sathyendranath et al., 2001) according to:

$$F_{pico,nano} = \frac{C_{pico,nano}^m \left[1 - exp\left(-\frac{D_{pico,nano}}{C_{pico,nano}^m}[Chl\text{-}a]\right)\right]}{[Chl\text{-}a]}, \tag{9}$$

and

$$F_{pico} = \frac{C_{pico}^m \left[1 - exp\left(-\frac{D_{pico}}{C_{pico}^m}[Chl\text{-}a]\right)\right]}{[Chl\text{-}a]}, \tag{10}$$

where the model parameters $C^m_{pico,nano}$ and C^m_{pico} represent asymptotic maximum [Chl-a] for the associated size classes, and $D_{pico,nano}$ and D_{pico} represent the fraction of each size class as [Chl-a] tends toward zero. Model parameters are determined by fitting Eqs. 9 and 10 to an *in situ* data set of $F_{pico,nano}$, F_{pico}, and [Chl-a] via nonlinear least squares regression. F_{micro} and F_{nano} are then determined as F_{micro} = 1 - $F_{pico,nano}$ and F_{nano} = $F_{pico,nano}$ - F_{pico}, respectively. Brewin et al. (2010) used a data set of HPLC pigments from the Atlantic Ocean ($N = 1935$) (Atlantic Meridional Transect cruises 5-15) and estimated PSCs using DPA to derive model parameters. Brewin et al. (2015a) utilized a much larger global data set of surface HPLC measurements ($N = 5841$) to compute the model parameters. These two models are denoted B10 and B15 throughout the remainder of the text. For simplicity, the notation B10 is also used to refer to the general framework that

underlies both of these models (i.e., Eqs. 9 and 10), in addition to the parameterization specific to that study. Further, while Brewin et al. (2015a) also investigated the influence of average irradiance in the mixed layer on model parameters, in this study B15 refers to the model without this modification. Parameter values obtained from the different studies are provided in Table 2.

2.7.1.2. Brewin et al. (2017)

Brewin et al. (2017) used a merged *in situ* HPLC/SFF data set from the North Atlantic ($N = 2239$) to compute the parameters of the B10 model (Eqs. 9 and 10). They then modified the model parameters to vary as a function of *SST* by matching the *in situ* PSC data with satellite-derived *SST* and conducting a running fit of the model to the data binned by increasing *SST*. They represented the resulting relationships between *SST* and model parameters using logistic functions, such that $C^m_{pico,nano}$, C^m_{pico}, $D_{pico,nano}$ and D_{pico} are expressed as:

$$C^m_{pico,nano} = 1 - \{\frac{G_1}{1 + \exp\left[-G_2(SST - G_3)\right]} + G_4 , \qquad (11)$$

$$C^m_{pico} = 1 - \{\frac{H_1}{1 + \exp\left[-H_2(SST - H_3)\right]} + H_4 , \qquad (12)$$

$$D_{pico,nano} = \frac{J_1}{1 + \exp\left[-J_2(SST - J_3)\right]} + J_4 , \qquad (13)$$

and

$$D_{pico} = \frac{K_1}{1 + \exp\left[-K_2(SST - K_3)\right]} + K_4 , \qquad (14)$$

where G_i, H_i, J_i, and K_i (where $i = $ 1-4) are empirical parameters controlling the shape of the respective logistic curve and are provided in Table 4 of Brewin et al. (2017). In the remainder of this text, the notation B17 is used to refer to the *SST-*

independent parameterization of the model, which uses a single set of model parameters derived from their full data set (Table 4). The *SST*-dependent parameterization, which uses Equations 11-14 with the published coefficients, is denoted as B17-*SST*.

2.7.1.3. Devred et al. (2011)

The model of Devred et al. (2011) (denoted D11) is based on the same exponential functions as the B10 model (Eqs. 9 and 10). The primary difference is that the model parameters $C^m_{pico,nano}$ and C^m_{pico} were not derived from HPLC pigment-based size classes, but rather by successive application of the two-population absorption model of Devred et al. (2006) to $a_{ph}(\lambda)$ and [*Chl-a*] data from the Northwest Atlantic and NASA's NOMAD data set. While the model was originally applied as a spectral-based approach, in this study it is implemented as an abundance-based method, using the parameters provided in Table 2 of Brewin et al. (2015a). In a comparison of nine existing PSC algorithms in the Northwest Atlantic region near Newfoundland, Liu et al. (2018) found the application of the this model as an abundance-based method to be the most successful (Model E in their study). The reader is referred to Chapter 4 of IOCCG (2014) for more information on this approach.

2.7.1.4. Hirata et al. (2011)

The empirical model of Hirata et al. (2011) (denoted H11) estimates the fractional contribution of pico- and microplankton to [*Chl-a*] with the equations:

$$F_{pico} = -[a_1 + exp(a_2 X + a_3)]^{-1} + a_4 X + a_5 , \qquad (15)$$

and

$$F_{micro} = [b_1 + exp(b_2 X + b_3)]^{-1} , \qquad (16)$$

where a_i and b_i (where $i = 1$-5 and $i = 1$-3, respectively) are empirical coefficients specific to each size class and X is log10-transformed [*Chl-a*]. F_{nano} is then calculated by difference (1 - F_{micro} - F_{pico}). The H11 model was developed using PSCs derived from a global HPLC data set ($N = 2776$) following a unique version of DPA that attributes [*TChl-b*] to nanoplankton rather than picoplankton, as in Brewin et al. (2010, 2015a, 2017) and the present study (see Section 2.6).

2.7.1.5. Moore and Brown (2020)

The model of Moore and Brown (2020) utilizes the H11 microplankton equation (Eq. 16) to estimate both F_{pico} and F_{micro}. Using a data set of surface HPLC pigments from the Atlantic Ocean ($N = 1083$), they developed two separate models: one parameterized using the DPA method [following the procedure of Brewin et al. (2015a)] and one parameterized using CHEMTAX (Mackey et al., 1996). They then incorporated different remotely sensed environmental variables into the models, following a similar approach to that of Brewin et al. (2015a, 2017), and created a look-up table (LUT) for each model parameter indexed by the environmental data. Of the environmental variables tested, they found that the inclusion of *SST* resulted in the largest reduction of model error. In this study, the DPA version of the model was applied, both with and without the incorporation of *SST*. The *SST*-independent model (denoted MB20) was applied using Eq. (16)

27

with the coefficients provided in Table 4 of Moore and Brown (2020). The *SST*-dependent model (denoted MB20-*SST*) was applied using the set of parameters from their LUT indexed by *SST* (obtained from Timothy Moore via personal communication).

2.7.1.6. Re-parameterized B10 and H11 Models

New model parameters for the B10 and H11 models were computed using the pigment-based estimates of F_{size} from the NES parameterization data set ($N = 418$), (Table 4). To re-parameterize the B10 model, Eqs. (9) and (10) were fit to $F_{pico,nano}$, F_{pico}, and C_{HPLC} using a nonlinear least squares curve fitting procedure (MATLAB function *lsqcurvefit.m*, Levenberg-Marquardt algorithm) with bootstrapping (Brewin et al., 2017; Brewin et al., 2015a; Efron, 1979). This involved

Table 4. Parameter values for the abundance-based models of Brewin et al. (2010) (Eqs. 9 and 10) and Hirata et al. (2011) (Eq. 16), obtained from this study and from previous studies.

Study	Geographic region	Years	Parameters for Equations (9) and (10)					
				$C^m_{pico,nano}$	C^m_{pico}	$D_{pico,nano}$	D_{pico}	
Brewin et al. (2010)	Atlantic	1997-2004	-	1.06	0.11	0.90	0.73	-
Brewin et al. (2015)	Global	1992-2012	-	0.77	0.13	0.94	0.91	-
Brewin et al. (2017)[a]	N Atlantic	1995-2015	-	0.82	0.13	0.87	0.73	-
Devred et al. (2011)	NW Atlantic	1996-2003	-	0.55	0.15	1.00	1.00	-
This Study	NES	2003-2018	-	0.81	0.15	0.78	0.54	-

Study	Geographic region	Years	Parameters for Equation (16)					
			$b_{1,micro}$	$b_{2,micro}$	$b_{3,micro}$	$b_{1,pico}$	$b_{2,pico}$	$b_{3,pico}$
Hirata et al. (2011)[b]	Global	1995-2008	0.91	-2.73	0.40	-	-	-
Moore and Brown (2020)[c]	Atlantic	1997-2014	0.82	-1.33	0.39	1.41	2.82	1.72
This Study	NES	2003-2018	1.03	-1.68	-0.12	-3.45	0.67	2.29

[a] Refers to the *SST*-independent model from their study
[b] Hirata et al. (2011) used a different empirical formula to estimate picoplankton (Eq. 15; see their Table 2)
[c] Refers to coefficients derived using the DPA method [see Table 4 of Moore and Brown (2020)]

randomly sub-sampling the data with replacement 1000 times, and re-fitting the model for each sub-sample, resulting in a parameter distribution from which the median value was taken as the new model parameter. Using the same procedure to re-parameterize the H11 model, both Eq. (15) and Eq. (16) were fit to F_{pico} and C_{HPLC}, and better results were found (not shown) when using the simpler logistic equation (Eq. 16), consistent with the findings of Moore and Brown (2020). Therefore, Eq. (16) was fit to both F_{micro} and F_{pico} and C_{HPLC} to derive new model parameters. These regionally re-parameterized abundance-based models are denoted B-NES and H-NES, respectively.

2.7.1.7. Regional SST-modified B10 Model

Following a similar methodology to recent studies (Brewin et al., 2019, 2017; Moore and Brown, 2020; Sun et al., 2019), the influence of SST on the parameters of the B10 model was investigated. This was done by sorting the pigment-based estimates of F_{pico} and $F_{pico,nano}$ from the parameterization data set ($N = 418$) by increasing SST and conducting a running fit of the model from low to high $SST,$ using a bin size of 125 samples. Starting at the lowest temperature, the bin was moved at one-sample intervals, and at each interval Eqs. (9) and (10) were fit to the data within the bin using a nonlinear least squares curve-fitting method with bootstrapping (as described in Section 2.7.1.6). From each fit, the median values of the model parameters C^m_{size} and D_{size} from the bootstrap distribution along with the average SST of the binned data were incorporated into a LUT, and

subsequently smoothed using a 5-point running average (Fig. 4). A LUT approach was chosen (Moore and Brown, 2020) rather than fitting logistic functions to represent the *SST*-parameter relationships (Brewin et al., 2017) in order to capture variability in the relationships that may be ecological meaningful and would
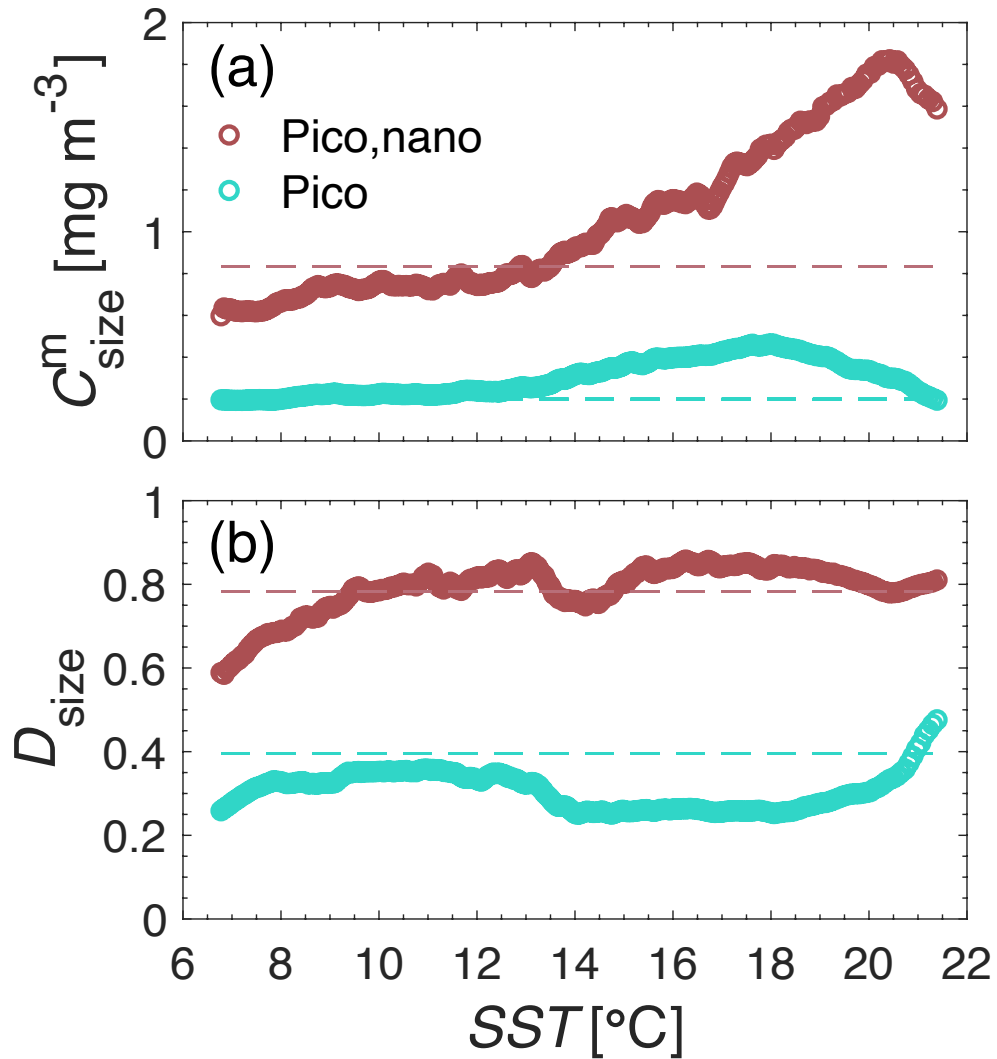
Figure 4. Brewin et al. (2010) model parameters (a) $C^m_{pico,nano}/C^m_{pico}$, and (b) $D_{pico,nano}/D_{pico}$ as a function of *SST*. Open circles show the median parameter values obtained by performing a running bootstrap fit of the model (Eqs. 9 and 10) to the *in situ* parameterization data set (N = 418) sorted by increasing *SST*. The *SST*-parameter relationships were smoothed using a 5-point running average. Dashed lines indicate the *SST*-independent model (B-NES) parameters obtained when fitting the model to the full parameterization data set.

otherwise be smoothed out by a logistic curve. The LUT included 293 unique sets of model parameters covering a range of *SST* of ~6.8 – 21.4 ℃ at intervals of ~0.06 ℃. Application of the LUT enables a dynamic set of model parameters based on remotely sensed *SST*. This *SST*-dependent re-parameterization is denoted B-NES-*SST* henceforth.

2.7.2. Absorption-Based

2.7.2.1. Ciotti et al. (2002)

The model of Ciotti et al. (2002) (denoted C02) estimates the fractional contribution of picoplankton (F_{pico}), by weighting $a_{ph}^*(\lambda)$ between two basis spectra representing "pure" micro- and picoplankton. The basis spectra were determined by lab measurements of $a_{ph}(\lambda)$ of 16 natural phytoplankton communities of varying dominant cell sizes, and are provided in Ciotti et al. (2002), with an updated picoplankton spectra provided by Ciotti and Bricaud (2006). The model can be expressed as:

$$a_{ph}^*(\lambda) = \left[F_{pico} \ * \ \bar{a}_{pico}^*(\lambda)\right] + \left[\left(1 - F_{pico}\right) \ * \ \bar{a}_{micro}^*(\lambda)\right], \qquad (13)$$

where $\vec{a}^*_{pico}(\lambda)$ and $\vec{a}^*_{micro}(\lambda)$ represent the basis spectra of pico- and microplankton, respectively. F_{pico} was estimated from Eq. (13) by performing a linear least squares optimization (MATLAB function *lsqlin.m*), using satellite-derived $a_{ph}^*(\lambda)$ (calculated by dividing the satellite $a_{ph}(\lambda)$ by the satellite [*Chl-a*]), and the published basis spectra at 443, 490, 510, and 555 nm (Fig. 5). Only these four wavelengths were used due to the poor retrieval of $a_{ph}(670)$ (see Section 3.1) and better statistical

performance when excluding 412 nm. The inverse of F_{pico} (1 - F_{pico}) was considered

equivalent to the combined fraction of micro- and nanoplankton ($F_{micro,nano}$).
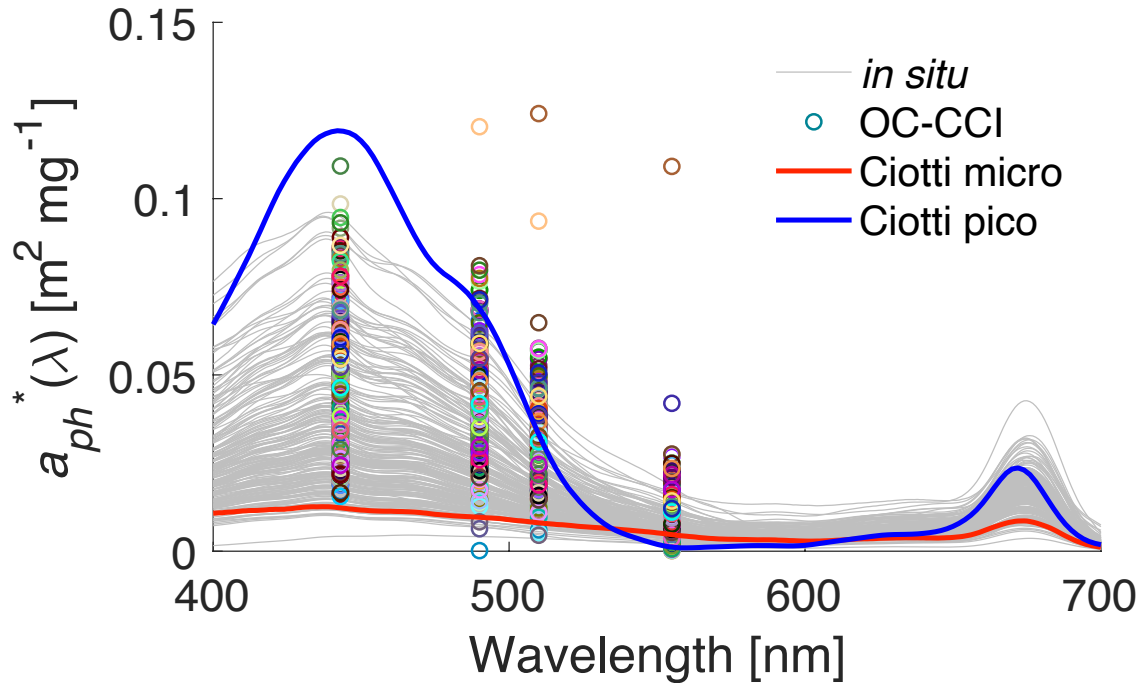
Figure 5. Satellite-derived $a_{ph}^*(\lambda)$ at 443, 490, 510, and 555 nm from the validation data set ($N = 368$; open circles) compared with the *in situ* $a_{ph}^*(\lambda)$ spectra ($N = 214$; gray lines) and the micro- and picoplankton basis spectra from the model of Ciotti et al. (2002) (red and blue lines, respectively).

2.7.2.2. Mouw and Yoder (2010)

The algorithm of Mouw and Yoder (2010) (denoted MY10) employs an

optical LUT containing ranges of F_{micro} (binned to increments of 0.1), [*Chl-a*], and

$a_{dg}(443)$, from which $R_{rs}(\lambda)$ was calculated using the radiative transfer software

HydroLight (Mobley and Sundman, 2013). The model uses satellite [*Chl-a*] and

$a_{dg}(443)$ as inputs to first narrow the search space of the LUT, then the closest

matching LUT $R_{rs}(\lambda)$ to the satellite-derived $R_{rs}(\lambda)$ is found to retrieve the

corresponding F_{micro}. $F_{pico,nano}$ is then calculated as 1 - F_{micro}. Based on determined

thresholds for the detectability of cell size from SeaWiFS $R_{rs}(\lambda)$ (Mouw and Yoder,

2010), the algorithm masks pixels with [Chl-a] < 0.05 mg m^{-3}, [Chl-a] > 1.75 mg m^{-3}, or $a_{dg}(443)$ > 0.17. Additionally, when applied to a satellite image, a 2D-

averaging filter (MATLAB function *filter2.m*) with a 3x3 pixel size is applied in the

algorithm routine.

2.8. Model Assessment and Imagery Application

PSC algorithm performance was assessed statistically (see Section 2.5) as

follows. First, using the *in situ* [Chl-a] data as input, estimates of F_{size} and C_{size} from

the *SST*-independent abundance-based models (B10, B15, B17, D11, H11, MB20,

B-NES, and H-NES) were compared with the *in situ* pigment-based estimates of

F_{size} and C_{size} for both the parameterization and validation data sets. Then, using

the *in situ* [Chl-a] and matching satellite *SST* as input, estimates of F_{size} and C_{size}

from the *SST*-dependent models (B17-*SST*, MB20-*SST*, B-NES-*SST*) were also

compared with the *in situ* F_{size} and C_{size} for both the parameterization and validation

data sets, and the influence of *SST* on model performance relative to the *SST*-

independent models was quantified. Lastly, using the satellite-derived data as

input, independent satellite validation of C_{size} was conducted for the regionally re-

parameterized abundance-based models (B-NES-*SST*, B-NES, and H-NES) and

the absorption-based algorithms (C02 and MY10).

To illustrate the application of the models to ocean color imagery and

preliminarily explore spatial-seasonal variations of PSCs in the NES region, the

best validating abundance-based and absorption-based models were applied to monthly imagery composites for April 2019 and September 2019, and qualitatively compared. A more comprehensive long-term analysis of the spatial-temporal variability of PSCs in the NES region will be presented in a separate publication.

3.   RESULTS

3.1.   Satellite Validation of [*Chl-a*], $a_{ph}(\lambda)$ and $a_{dg}(\lambda)$

As the performance of PSC algorithms is largely dependent on the quality of the satellite products used as inputs, the satellite retrievals of [*Chl-a*], $a_{ph}(\lambda)$ and $a_{dg}(\lambda)$ in the NES study region were first validated. Of the two [*Chl-a*] algorithms assessed, the standard OC-CCI algorithm (Fig. 6a) displayed lower error and bias (*MAE* = 0.21, δ = -0.03) than the regional empirical algorithm of Pan et al. (2010) (*MAE* = 0.27, δ = -0.20; Fig. 6b) when compared with the *in situ* HPLC [*Chl-a*]. The OC-CCI algorithm was associated with overestimation at low [*Chl-a*] and underestimation at high [*Chl-a*] (>0.6 mg m^{-3}). This is a relatively common feature of [*Chl-a*] estimated from empirical band-ratio algorithms (i.e., OCx), that can be attributed primarily to the impact of phytoplankton cell size and underlying variability in the concentrations of CDOM and inorganic particulates (Dierssen, 2010; Mouw et al., 2012; Sauer et al., 2012). In contrast, the algorithm of Pan et al. (2010) exhibited a considerable systematic underestimation across the entire [*Chl-a*] range (δ = -0.20). This difference is reflected in a lower Type-II regression slope for the OC-CCI algorithm (*S* = 0.66) compared with a slope nearer to one for the Pan et al. (2010) algorithm (*S* = 0.89). The two algorithms displayed similar correlation coefficients (*r* = 0.75 and 0.74 respectively). The performance of the OC-CCI algorithm in the NES was comparable to the global [*Chl-a*] validation of OC-CCI v4.2 as shown in the Product User Guide (*RMSE* = 0.32, δ = 0.07, *r* = 0.75, *S* = 0.72; see their Figure 5). Considering the lower error and bias of the OC-

35

Figure 6. Bivariate histograms showing the satellite-to-*in situ* comparisons of [*Chl-a*], $a_{ph}(\lambda)$, and $a_{dg}(\lambda)$, shaded by number of observations: (a) [*Chl-a*] from the standard OC-CCI algorithm, (b) [*Chl-a*] from the regional algorithm of Pan et al. (2010), (c) $a_{ph}(443)$, (d) $a_{ph}(490)$, (e) $a_{ph}(510)$, (f) $a_{dg}(443)$, (g) $a_{dg}(490)$, and (h) $a_{dg}(510)$ from the standard OC-CCI algorithm (QAA_v5). The solid black line is the 1:1 line, dashed black lines indicate the 1:1 line $\pm$ 30%, and the red line is the Type-II regression line. *N* denotes the number of match-ups, *MAE* denotes the mean absolute error, δ denotes the bias, *r* denotes the correlation coefficient, and *S* denotes the regression slope. The $a_{ph}(\lambda)$ and $a_{dg}(\lambda)$ data are shown using the same x- and y-axis range for comparison.

36

CCI [*Chl-a*] algorithm, [*Chl-a*] from this algorithm was used as the satellite input to the PSC models in this study.

The standard OC-CCI estimates of $a_{ph}(\lambda)$ and $a_{dg}(\lambda)$, derived using QAA_v5, compared reasonably with *in situ* measurements, with most points falling within the $\pm 30\%$ uncertainty range at the wavelengths 443, 490, and 510 nm (Fig. 6 c-h). The lowest errors for $a_{ph}(\lambda)$ were observed at 490 and 510 nm ($MAE = 0.22$ and 0.24, respectively), with retrievals of $a_{ph}(443)$ exhibiting slightly higher error ($MAE = 0.28$). For $a_{dg}(\lambda)$, the best performance was observed at 443 nm ($MAE = 0.17$, $\delta = -0.14$). There was a consistent negative bias in the retrieved $a_{dg}(\lambda)$ which became more negative at longer wavelengths, corresponding with an increasingly positive bias for $a_{ph}(\lambda)$. Retrievals of $a_{ph}(555)$ and $a_{ph}(670)$ were associated with larger errors ($MAE = 0.32$ and 0.62, respectively), the same being true for $a_{dg}(555)$ and $a_{dg}(670)$ ($MAE = 0.38$ and 0.41, respectively). The decrease in performance at longer wavelengths for QAA_v5 is consistent with results from the global inter-comparison of bio-optical algorithms conducted by Brewin et al. (2015b) (Model E in their study). Considering the reasonable performance of the standard OC-CCI $a_{ph}(\lambda)$ and $a_{dg}(443)$ products (443 nm is the only wavelength required for $a_{dg}(\lambda)$ as input into the MY10 algorithm), no regional optimization of these products was attempted in this study.

3.2. Comparison of *SST*-independent Abundance-based Models

Figure 7 shows the *in situ* pigment-based estimates of F_{size} and C_{size} from the parameterization data set ($N = 418$) with the *SST*-independent abundance-

based models overlain. F_{size} and C_{size} exhibited trends with C_{HPLC} that are consistent with established relationships of phytoplankton size structure and total biomass (Uitz et al., 2006; Brewin et al., 2010; Hirata et al., 2011). F_{micro} generally increased, while $F_{pico,nano}$, and F_{pico} generally decreased with increasing C_{HPLC}. F_{nano} displayed a unimodal relationship C_{HPLC}, peaking at intermediate C_{HPLC}. C_{micro} increased in near log-linear fashion with C_{HPLC}, becoming more tightly correlated at higher C_{HPLC}, when microplankton are the dominant size class. $C_{pico,nano}$, C_{nano}, and C_{pico}, also displayed an overall positive relationship with C_{HPLC}, with more variability at higher C_{HPLC}.

The abundance-based models all followed to first order these general trends, with some variations that can be attributed to differences in the model frameworks, data sets, and approaches used for model development/parameterization. For example, the B10 model parameters $C^m_{pico,nano}$ and C^m_{pico} impose asymptotic maximums to $C_{pico,nano}$ and C_{pico} respectively, while the purely empirical H11 model does not impose any strict maximums. This can be seen when comparing C_{pico} predicted by the H-NES model, which increases continuously with C_{HPLC}, with that of the B-NES model, which levels off at the imposed maximum concentration ($C^m_{pico} = 0.2$ mg m^{-3}) (Fig. 7h). The H11-modeled F_{pico} is based on a different empirical function (Eq. 15) than the one used in this study (see Section 2.7.1.5), and goes to zero at $C_{HPLC} > 4$ mg m^{-3} (Fig. 7d), accounting for the breakdown in this model at higher C_{HPLC} for C_{pico}, C_{nano}, and $C_{pico,nano}$ (Fig. 7f-h). Compared with the other models examined, the B-NES model
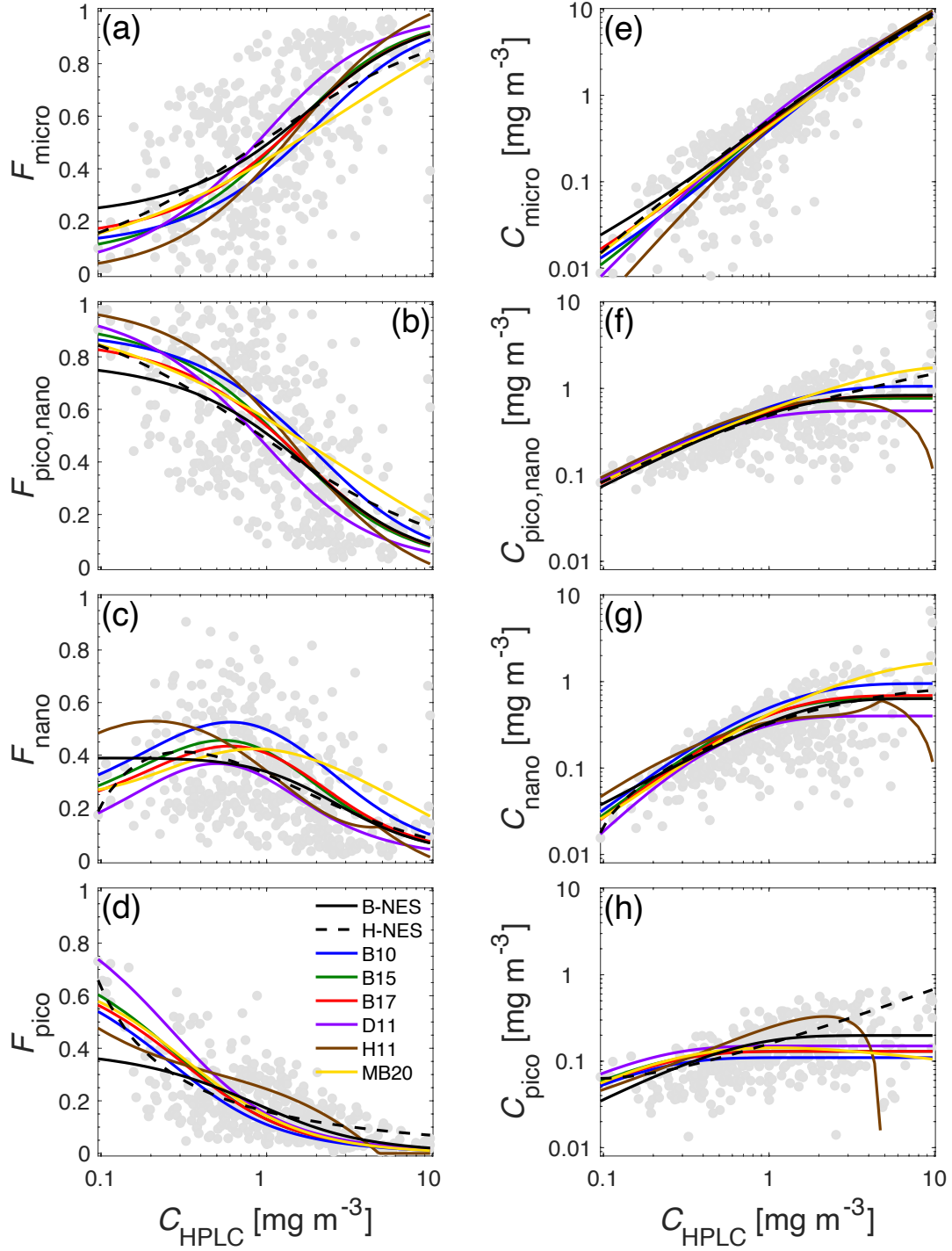
Figure 7. Pigment-based estimates of F_{size} (a-d) and C_{size} (e-h) as a function of C_{HPLC} from the parameterization data set ($N = 418$) with abundance-based models overlain: re-parameterized B10 model (B-NES, solid black), re-parameterized H11 model (H-NES, dashed black), Brewin et al., 2010 (B10, blue), Brewin et al., 2015a (B15, green), Brewin et al., 2017 (B17, red), Devred et al., 2011 (D11, violet), Hirata et al., 2011 (H11, brown), and Moore and Brown, 2020 (MB20, yellow).

Table 5. Statistical metrics obtained when comparing the *in situ* pigment-based estimates of F_{size} and C_{size} from the parameterization and validation data sets with estimates from the abundance-based models shown in Figure 7. Statistical calculations were performed in linear space for F_{size} and $\log_{10}$ space for C_{size}. Metrics for C_{size} are shown in parentheses.

Parameter	Model	in situ parameterization set (N = 418)			in situ validation set (N = 368)		
		MAE	δ	r	MAE	δ	r
F_{micro} (C_{micro})	B-NES	0.18 (0.24)	0.01 (0.11)	0.56 (0.86)	0.19 (0.25)	0.01 (0.13)	0.44 (0.85)
	H-NES	0.18 (0.21)	0.00 (0.10)	0.55 (0.86)	0.19 (0.25)	0.01 (0.12)	0.46 (0.85)
	B10	0.19 (0.24)	-0.08 (0.00)	0.56 (0.86)	0.21 (0.26)	-0.08 (0.01)	0.44 (0.85)
	B15	0.18 (0.24)	-0.02 (0.05)	0.56 (0.86)	0.20 (0.25)	-0.04 (0.05)	0.45 (0.85)
	B17	0.18 (0.24)	-0.02 (0.07)	0.56 (0.86)	0.19 (0.25)	-0.02 (0.08)	0.44 (0.85)
	D11	0.19 (0.24)	0.03 (0.10)	0.55 (0.86)	0.19 (0.25)	0.02 (0.09)	0.45 (0.85)
	H11	0.19 (0.25)	-0.06 (-0.02)	0.56 (0.86)	0.21 (0.25)	-0.08 (-0.04)	0.44 (0.85)
	MB20	0.19 (0.24)	-0.06 (0.04)	0.55 (0.86)	0.20 (0.25)	-0.05 (0.06)	0.45 (0.85)
$F_{pico,nano}$ ($C_{pico,nano}$)	B-NES	0.18 (0.19)	-0.01 (0.06)	0.56 (0.67)	0.19 (0.20)	-0.01 (0.06)	0.44 (0.72)
	H-NES	0.18 (0.19)	-0.01 (0.06)	0.55 (0.67)	0.19 (0.19)	-0.01 (0.07)	0.46 (0.73)
	B10	0.19 (0.21)	0.08 (0.14)	0.56 (0.67)	0.21 (0.22)	0.08 (0.14)	0.44 (0.72)
	B15	0.18 (0.20)	0.03 (0.09)	0.56 (0.66)	0.20 (0.21)	0.04 (0.10)	0.45 (0.71)
	B17	0.18 (0.19)	0.02 (0.08)	0.56 (0.66)	0.19 (0.20)	0.02 (0.09)	0.44 (0.71)
	D11	0.19 (0.20)	-0.03 (0.01)	0.55 (0.65)	0.19 (0.20)	-0.02 (0.03)	0.45 (0.70)
	H11	0.19 (0.22)	0.06 (0.09)	0.56 (0.47)	0.21 (0.22)	0.08 (0.12)	0.44 (0.68)
	MB20	0.19 (0.20)	0.06 (0.14)	0.55 (0.67)	0.20 (0.20)	0.05 (0.13)	0.45 (0.73)
F_{nano} (C_{nano})	B-NES	0.15 (0.24)	0.00 (0.10)	0.37 (0.66)	0.17 (0.28)	0.01 (0.13)	0.12 (0.74)
	H-NES	0.14 (0.24)	-0.01 (0.10)	0.38 (0.67)	0.16 (0.28)	0.00 (0.12)	0.16 (0.72)
	B10	0.18 (0.29)	0.12 (0.25)	0.37 (0.66)	0.21 (0.32)	0.13 (0.27)	0.20 (0.74)
	B15	0.15 (0.25)	0.05 (0.16)	0.38 (0.66)	0.17 (0.29)	0.05 (0.19)	0.20 (0.74)
	B17	0.15 (0.25)	0.04 (0.15)	0.37 (0.66)	0.17 (0.28)	0.04 (0.18)	0.20 (0.74)
	D11	0.14 (0.24)	-0.04 (0.02)	0.39 (0.65)	0.16 (0.26)	-0.04 (0.05)	0.21 (0.73)
	H11	0.16 (0.26)	0.02 (0.09)	0.36 (0.55)	0.19 (0.30)	0.04 (0.15)	0.10 (0.73)
	MB20	0.17 (0.27)	0.07 (0.21)	0.26 (0.67)	0.18 (0.29)	0.06 (0.21)	0.18 (0.74)
F_{pico} (C_{pico})	B-NES	0.08 (0.21)	-0.01 (0.05)	0.61 (0.55)	0.10 (0.22)	-0.02 (0.04)	0.63 (0.54)
	H-NES	0.07 (0.21)	0.00 (0.09)	0.67 (0.53)	0.09 (0.21)	-0.01 (0.07)	0.73 (0.59)
	B10	0.08 (0.25)	-0.04 (-0.10)	0.63 (0.40)	0.10 (0.25)	-0.04 (-0.08)	0.71 (0.40)
	B15	0.08 (0.24)	-0.02 (-0.04)	0.63 (0.41)	0.10 (0.24)	-0.02 (-0.01)	0.70 (0.42)
	B17	0.08 (0.24)	-0.02 (-0.04)	0.63 (0.43)	0.10 (0.24)	-0.02 (-0.02)	0.70 (0.43)
	D11	0.09 (0.24)	0.01 (0.03)	0.63 (0.40)	0.10 (0.24)	0.02 (0.05)	0.71 (0.40)
	H11	0.09 (0.25)	0.05 (0.19)	0.62 (0.52)	0.11 (0.25)	0.04 (0.17)	0.64 (0.51)
	MB20	0.08 (0.24)	-0.01 (-0.02)	0.63 (0.34)	0.10 (0.24)	-0.01 (0.01)	0.70 (0.38)

predicted a slightly higher F_{micro} and lower $F_{pico,nano}$ and F_{pico} at low C_{HPLC} (Fig. 7a,b,d). Further, the B-NES-modeled F_{nano} leveled off at low C_{HPLC} rather than decreasing as with the other models (Fig. 7c). Despite the variability between the

different models, the range of variability in the pigment-based estimates of F_{size} and C_{size} was generally greater across the entire trophic domain. Statistical comparison between the *in situ* and modeled F_{size} and C_{size} for both the parameterization and validation data sets yielded very similar metrics between the models (Table 5). Overall, minimal improvement in performance was observed for the regionally re-parameterized models (B-NES and H-NES) compared with the other models examined, although there was a reduction in error and bias for the nanoplankton size class compared with the original global models (B10 and H11). This could in part be due to differences in the DPA methods used in the development of these models relative to the version used for model parameterization and validation in this study (see Section 2.7.1.4).

3.3. Regional *SST*-Dependent Model (B-NES-*SST*)

Figure 8 shows the modeled F_{size} and C_{size} from the B-NES-*SST* model as a function of [*Chl-a*] for different *SST*, along with the *SST*-independent model (B-NES) for reference. *SST* had a clear influence on the predicted F_{size} and C_{size} for all of the size classes. Lower *SST* was associated with a higher fraction of microplankton, and a lower fraction of nanoplankton and picoplankton (Fig. 8a-d), consistent with the results of previous studies (Brewin et al., 2017; Sun et al., 2019; Moore and Brown, 2020). This relationship was generally observed across the entire [*Chl-a*] domain, but was more pronounced at lower [*Chl-a*]. F_{nano} increased with *SST* for [*Chl-a*] > 1 mg m^{-3}, whereas for [*Chl-a*] < 1 mg m^{-3}, F_{nano} increased with *SST* only up to ~18 ºC, beyond which there was a decrease in F_{nano}
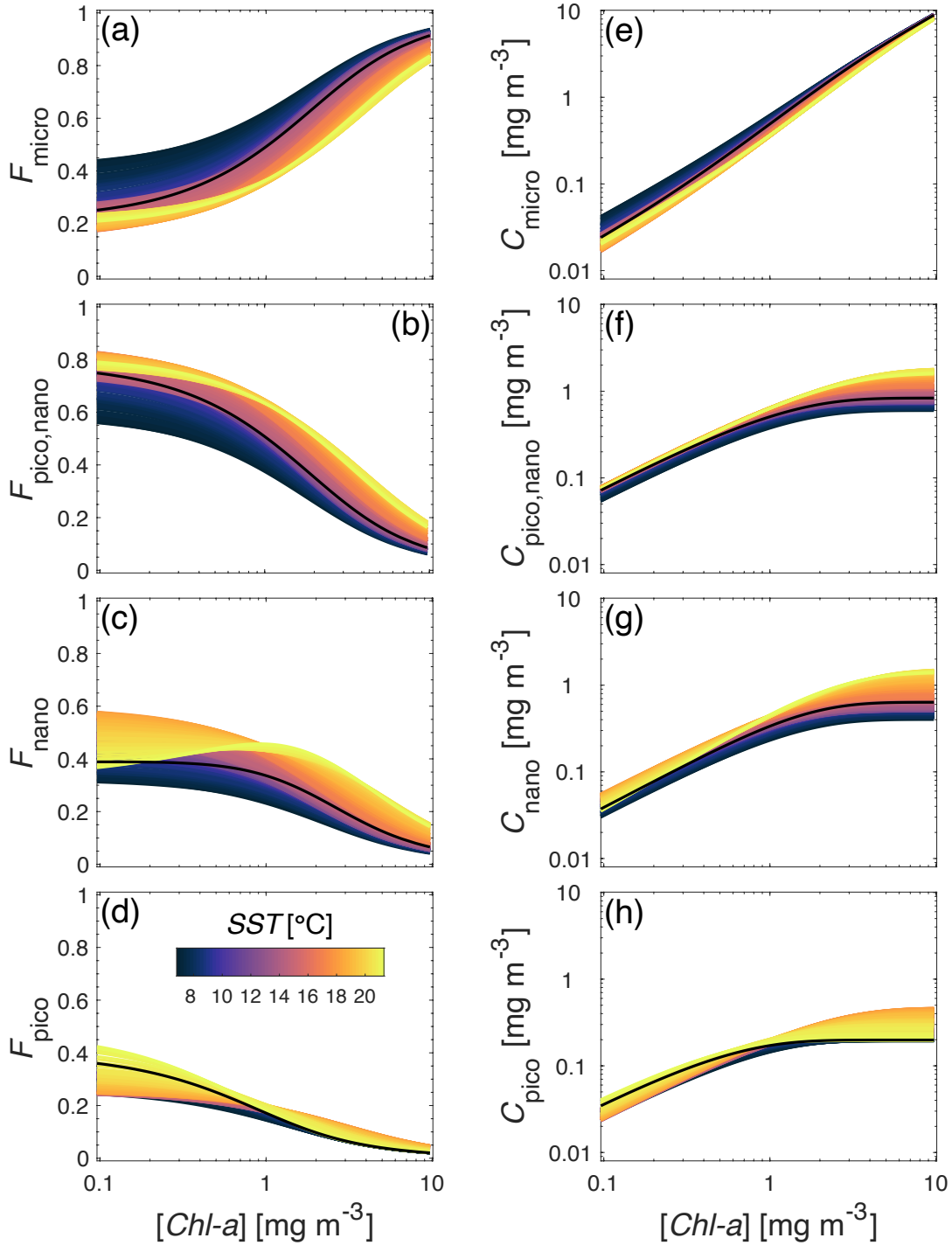
Figure 8. Modeled F_{size} (a-d) and C_{size} (e-h) from the B-NES-*SST* model plotted as a function of [*Chl-a*], with the color gradient illustrating the changes in the model when model parameters vary as a function of *SST* (see Section 2.7.1.7, Fig. 4). The black line indicates the *SST*-independent model, with a single set of model parameters (B-NES).

corresponding with an increase in F_{pico} at $SST > 18$ ºC. The largest variability in the modeled C_{micro} with SST was at $[Chl\text{-}a] < 1$ mg m^{-3}, whereas the largest variability in the modeled $C_{pico,nano}$, C_{nano}, and C_{pico} with SST was at $[Chl\text{-}a] > 1$ mg m^{-3} (Fig. 8e-h).

Results from the statistical comparison of modeled F_{size} and C_{size} from the B-NES-SST, B17-SST, and MB20-SST models with the *in situ* pigment-based estimates of F_{size} and C_{size} are presented in Table 6. For both the parameterization and validation data sets, the B-NES-SST model performed with lower error and significantly higher correlation coefficients than the other two SST-dependent models across all size classes. There was also a consistent improvement in performance (i.e., reduction in error, increase in correlation coefficient) for the B-NES-SST model relative to the SST-independent B-NES model for both data sets. Considering the statistical results from the validation set, the inclusion of SST led to a reduction in MAE of 10-12% for F_{size} and 4-10% for C_{size}, with the largest reductions for F_{nano} and $C_{pico,nano}$, respectively. Likewise, the inclusion of SST increased the correlation coefficient (r) for F_{size} and C_{size}, with the largest increases for F_{nano} and C_{pico}, respectively. Interestingly, the B17-SST model exhibited slightly worse performance relative to the SST-independent B17 model for estimating F_{micro}, $F_{pico,nano}$, and $C_{pico,nano}$, with essentially no change for C_{micro}. The MB20-SST model displayed general improvement over the MB20 model.

Table 6. Mean absolute error (*MAE*) and correlation coefficients (*r*) for F_{size} and C_{size} (values for C_{size} shown in parentheses) for the *SST*-dependent abundance-based models applied to the *in situ* parameterization and validation data sets. The percent change in the metrics when incorporating *SST* relative to the *SST*-independent models is included for reference. Percentages are rounded to the nearest 1%.

Parameter	Model	*in situ* parameterization set (N = 418)				*in situ* validation set (N = 368)			
		MAE	*% change with SST*	*r*	*% change with SST*	*MAE*	*% change with SST*	*r*	*% change with SST*
F_{micro} (C_{micro})	B-NES-*SST*	0.16 (0.21)	-11 (-13)	0.68 (0.89)	+21 (+3)	0.17 (0.24)	-11 (-4)	0.58 (0.87)	+32 (+2)
	B17-*SST*	0.19 (0.23)	+6 (-4)	0.54 (0.87)	-4 (+1)	0.20 (0.25)	+5 (0)	0.44 (0.85)	0 (0)
	MB20-*SST*	0.18 (0.23)	-5 (-4)	0.59 (0.83)	+7 (-3)	0.19 (0.24)	-5 (-4)	0.49 (0.86)	+9 (+1)
$F_{pico,nano}$ ($C_{pico,nano}$)	B-NES-*SST*	0.16 (0.17)	-11 (-11)	0.68 (0.75)	+21 (+12)	0.17 (0.18)	-11 (-10)	0.58 (0.77)	+32 (+6)
	B17-*SST*	0.19 (0.20)	+5 (+5)	0.54 (0.59)	-4 (-11)	0.20 (0.20)	+5 (0)	0.44 (0.72)	0 (+1)
	MB20-*SST*	0.18 (0.20)	-5 (0)	0.59 (0.56)	+7 (-16)	0.19 (0.19)	-5 (-5)	0.49 (0.73)	+9 (0)
F_{nano} (C_{nano})	B-NES-*SST*	0.13 (0.21)	-13 (-13)	0.55 (0.74)	+49 (+12)	0.15 (0.26)	-12 (-7)	0.39 (0.79)	+225 (+6)
	B17-*SST*	0.14 (0.24)	-7 (-4)	0.44 (0.66)	+19 (0)	0.16 (0.27)	-6 (-4)	0.29 (0.75)	+45 (+1)
	MB20-*SST*	0.16 (0.26)	-6 (-4)	0.28 (0.58)	+8 (-13)	0.16 (0.27)	-11 (-7)	0.18 (0.72)	0 (-3)
F_{pico} (C_{pico})	B-NES-*SST*	0.07 (0.19)	-13 (-10)	0.70 (0.64)	+15 (+16)	0.09 (0.20)	-10 (-9)	0.73 (0.62)	+16 (+15)
	B17-*SST*	0.08 (0.23)	0 (-4)	0.63 (0.46)	0 (+7)	0.09 (0.23)	-10 (-4)	0.73 (0.53)	+4 (+23)
	MB20-*SST*	0.08 (0.21)	0 (-13)	0.67 (0.53)	+6 (+56)	0.10 (0.22)	0 (-8)	0.72 (0.52)	+3 (+37)

3.4. Satellite Validation of C_{size}

Using the satellite data as input, estimates of C_{size} from the re-parameterized abundance-based models (B-NES-SST, B-NES, and H-NES) and absorption-based algorithms (C02 and MY10) were compared with the *in situ* pigment-based C_{size} from the independent validation data set (N = 368). The B-NES-SST, B-NES, and H-NES models displayed fairly similar statistical performance (Fig. 9), although the SST-dependent model performed considerably better across all statistical metrics for C_{micro} (Fig. 9a). The B-NES-SST model generally performed better than the SST-independent B-NES model, and was less constrained by static maximums for $C_{pico,nano}$, C_{nano}, and C_{pico} (Fig. 9 f-h, dashed green lines), particularly for C_{pico}, for which a substantial increase in the correlation coefficient was observed, consistent with previous studies (Brewin et al., 2017; Sun et al., 2019). Like the OC-CCI [*Chl-a*] input product, the satellite-estimated C_{size} from these models tended to be underestimated at higher concentrations and overestimated at low concentrations, especially for C_{nano} and C_{pico} below 0.1 mg m^{-3} and 0.05 mg m^{-3}, respectively.

The C02 and MY10 algorithms performed comparably to the re-parameterized abundance-based models (Fig. 10). The MY10 algorithm estimated C_{micro} and $C_{pico,nano}$ with similar errors as the B-NES-SST model, but with higher correlation coefficients (r = 0.74 and 0.63, respectively) and improved regression slopes (S = 0.97 and 0.89, respectively), although it is noted that the number of validation points was reduced from N = 368 to N = 352 and N = 332 for C02 and MY10, respectively. For the former, this was due to 16 match-ups with negative
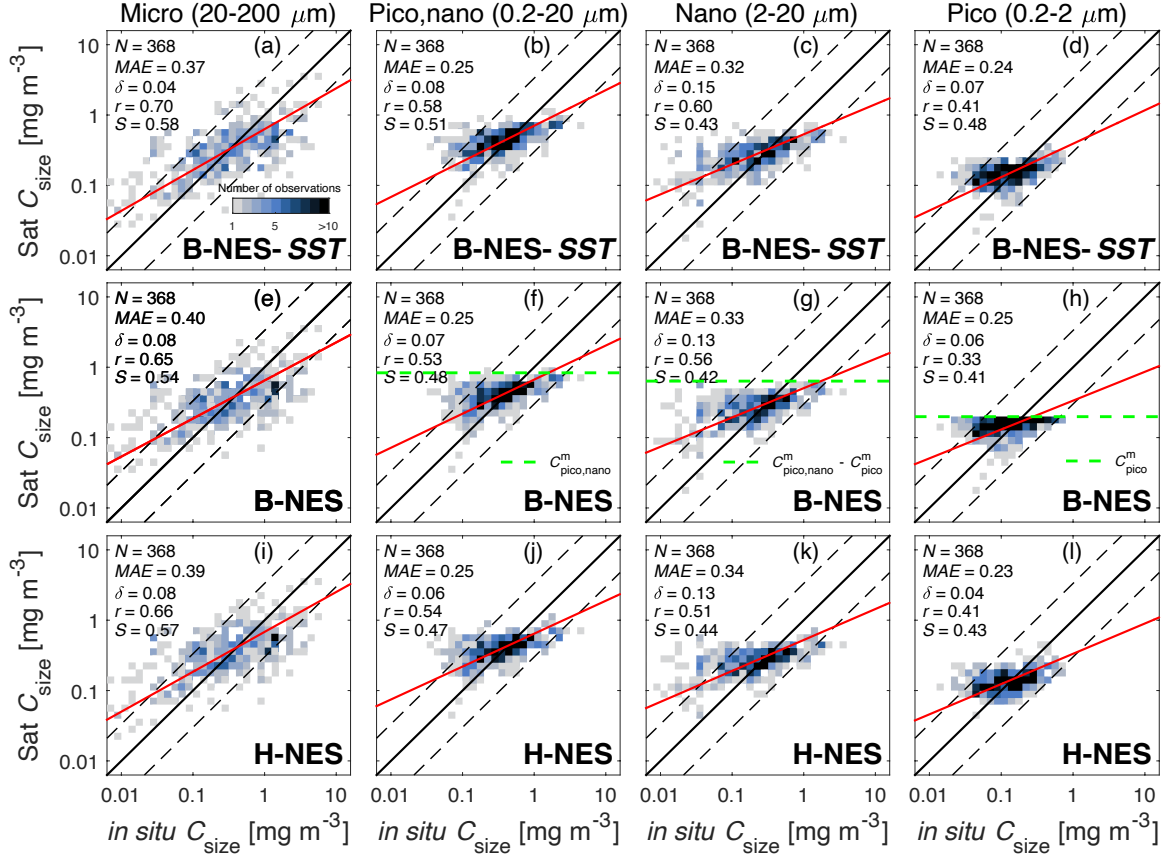
Figure 9. Bivariate histograms showing the satellite-to-*in situ* comparisons of C_{size} estimated from the regionally parameterized B-NES-*SST* (a-d), B-NES (a-d), and H-NES (i-l) abundance-based models, shaded by number of observations. The solid black line is the 1:1 line, dashed black lines indicate the 1:1 line ± 30%, and the red line is the Type-II regression line. Dashed green lines indicate the maximum chlorophyll concentrations imposed by the B-NES model. *N* denotes the number of match-ups for each parameter, *MAE* denotes the mean absolute error, δ denotes the bias, *r* denotes the correlation coefficient, and *S* denotes the regression slope.

satellite $a_{ph}(555)$ retrievals, while for the latter, 36 match-ups exceeded the [*Chl-a*] and $a_{dg}(443)$ detection thresholds of the MY10 algorithm (1.75 mg m^{-3} and 0.17 m^{-1}, respectively; see Sections 2.7.2.1 and 2.7.2.2). Although the overall bias was generally higher for the absorption-based approaches, they did not exhibit the same overestimation (underestimation) at low (high) concentrations as seen with

the abundance-based methods, with the exception of $C_{micro,nano}$ estimated by C02 model (Fig. 10a).
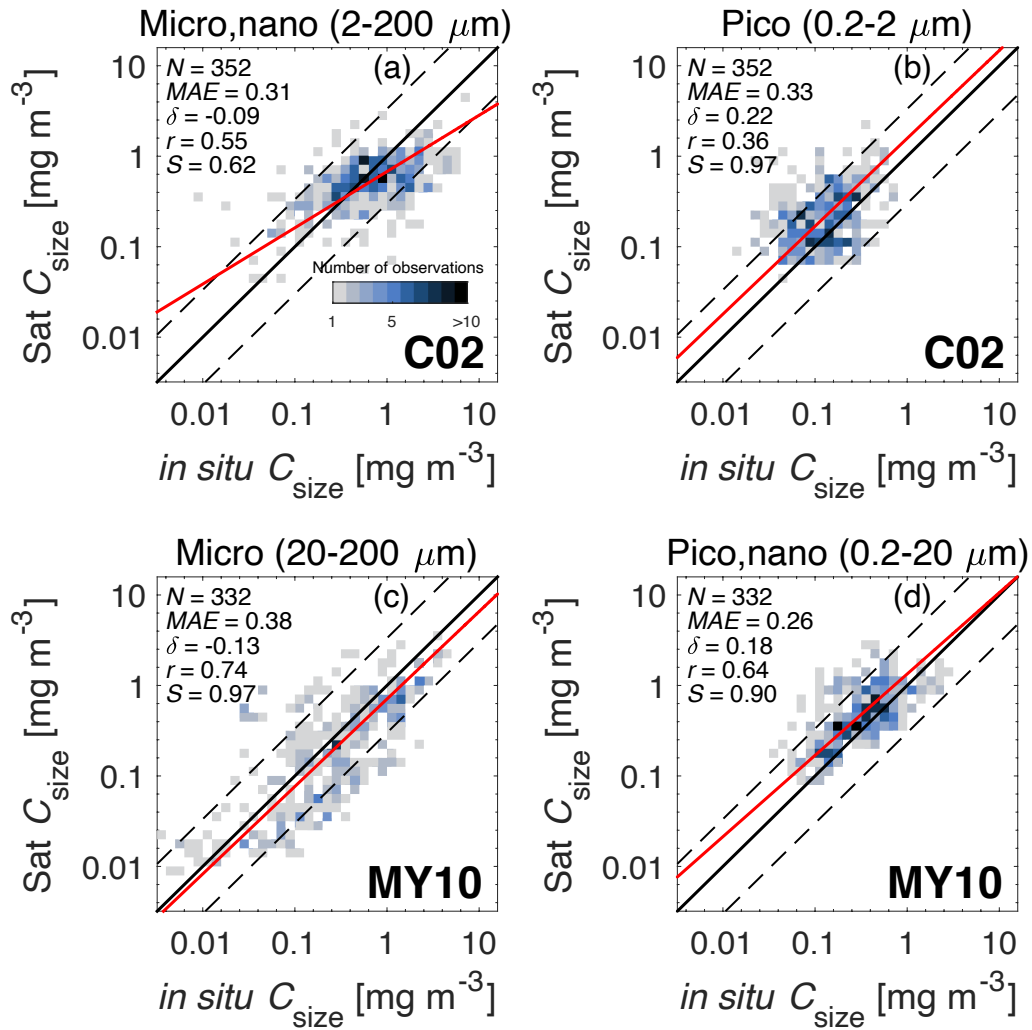
Figure 10. Bivariate histograms showing the satellite-to-*in situ* comparisons of C_{size} estimated from the absorption-based algorithms applied in this study: (a) $C_{micro,nano}$ and (b) C_{pico} from the algorithm of Ciotti et al. (2002) and (c) C_{micro} and (d) $C_{pico,nano}$ from the algorithm of Mouw and Yoder (2010). The solid black line is the 1:1 line, dashed black lines indicate the 1:1 line ± 30%, and the red line is the Type-II regression line. *N* denotes the number of match-ups, *MAE* denotes the mean absolute error, δ denotes the bias, *r* denotes the correlation coefficient, and *S* denotes the regression slope.

3.5. Examples of Satellite Imagery

Considering the overall improved performance of the B-NES-*SST* algorithm compared with the other abundance-based models, and the statistically similar validation metrics of the MY10 absorption-based approach, monthly composite imagery from these algorithms was generated for April 2019 and September 2019 for visualization and spatial-temporal comparison. These months were chosen as they were relatively cloud free and displayed contrasting *SST* and [*Chl-a*], thus providing some insight into the seasonal variability of phytoplankton size structure in the NES.

Figure 11 shows the monthly imagery of OC-CCI [*Chl-a*] (Fig. 11a) and MUR *SST* (Fig. 11b), along with the size class fractions (F_{micro}, F_{nano}, F_{pico}; Fig.11c-e) and size-specific [*Chl-a*] (C_{micro}, C_{nano}, C_{pico}; Fig.11f-h) from the B-NES-*SST* algorithm for April 2019. In April, around the time of the typical North Atlantic spring bloom (Friedland et al., 2016), [*Chl-a*] exceeding 1 mg m^{-3} was observed both on the shelf and off-shore, with the highest [*Chl-a*] observed around GB, south of Nova Scotia, and in the near-shore coastal waters along the MAB and GoM. *SST* ranged from <5 ºC in the northern GoM to ~25 ºC within the Gulf Stream. Microplankton were dominant in low *SST*, high [*Chl-a*] waters in the GoM, on GB, along the coast, and within the major estuaries. Nanoplankton were most prevalent in the intermediate [*Chl-a*] and *SST* waters off-shore. Picoplankton were the dominant size class in the oligotrophic, high *SST* surface waters of the Gulf of Stream.
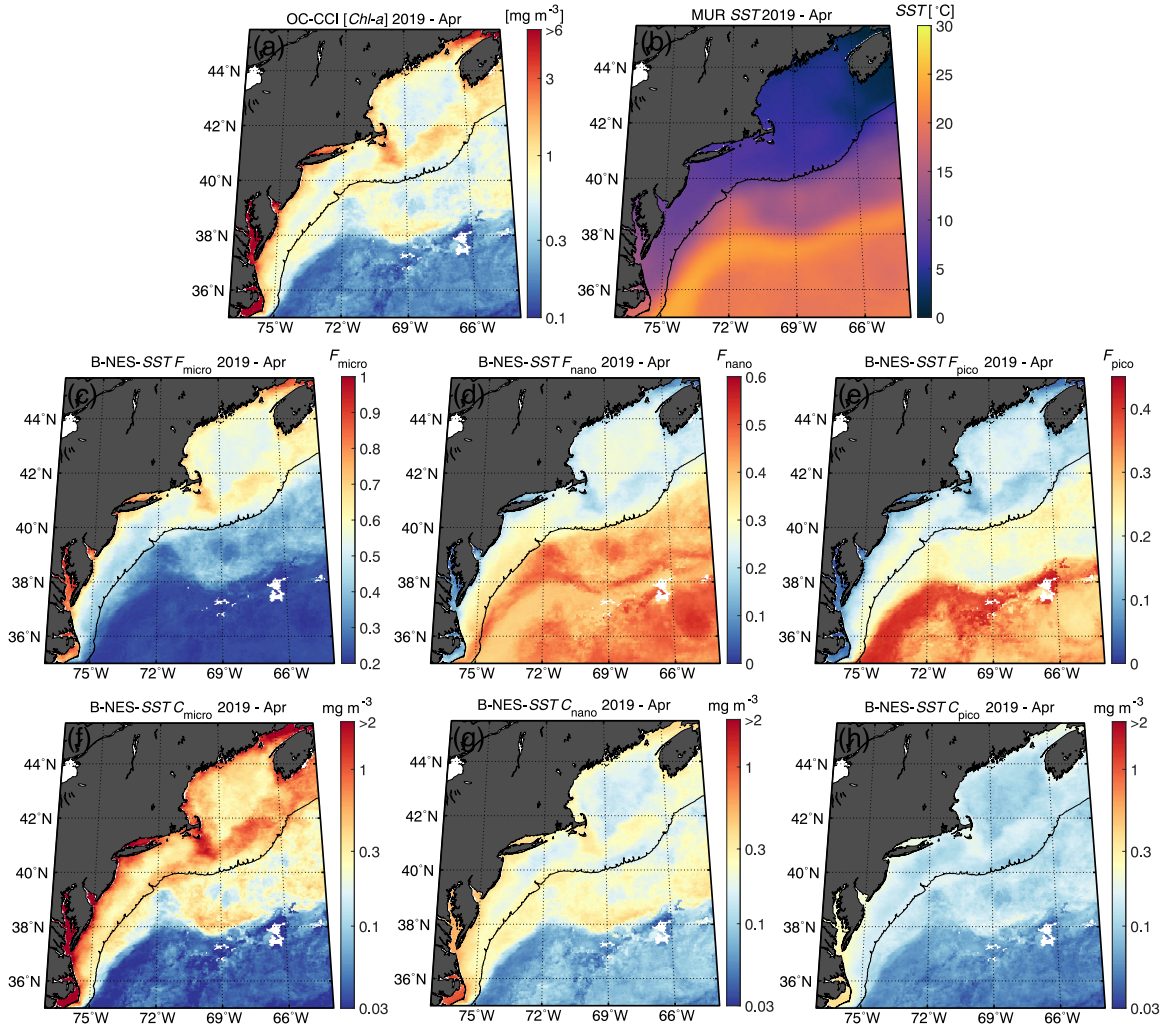
Figure 11. Monthly composite imagery for April 2019: (a) OC-CCI [*Chl-a*], (b) MUR *SST*, (c) F_{micro}, (d) F_{nano}, (e) F_{pico}, (f) C_{micro}, (g) C_{nano}, and (h) C_{pico} from the B-NES-*SST* model. Color scales for F_{size} are adjusted to reflect the range of the model for each size class (see Fig. 8). The black line indicates the 400 m isobath to mark the approximate location of the shelf break.

Figure 12 shows the same as Figure 11 but for September 2019. Compared with April, in September areas of [*Chl-a*] > 1 mg m^{-3} did not extend as far off-shore but were mainly confined to near-shore regions of the MAB, the GoM, and GB. There was a strong gradient in [*Chl-a*] from the highly productive waters along the

coast and to the north to the oligotrophic ([*Chl-a*] < 0.1 mg m⁻³) off-shore waters to

the south. *SST* exceeded 20 °C throughout much of the region, with cooler *SST*
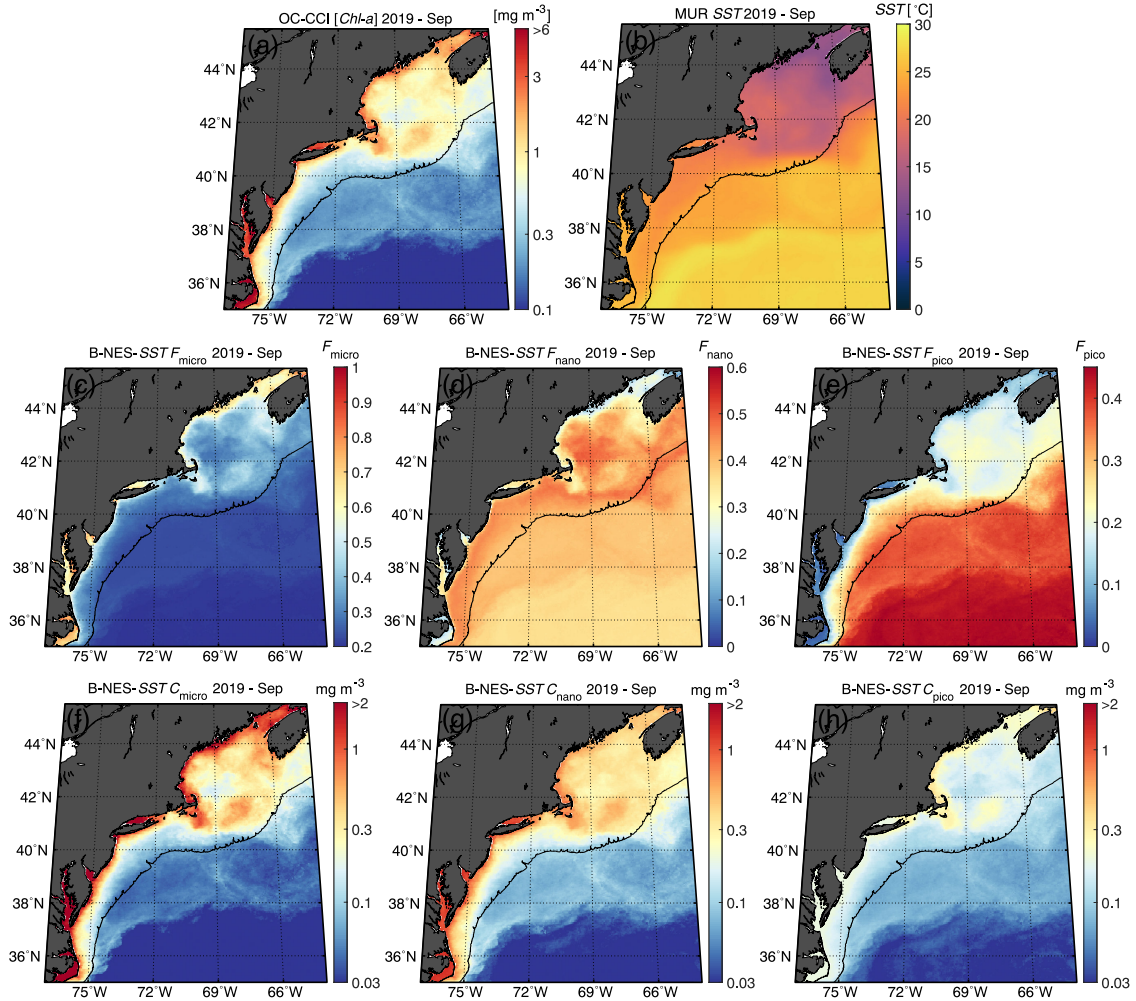
Figure 12. Same as Figure 11 but for September 2019.

observed to the north around GB and within the GoM, coinciding with the higher

[*Chl-a*] observed in these areas. Microplankton comprised a smaller fraction of

[*Chl-a*] in both near-shore and off-shore waters in September, with nanoplankton

becoming more dominant on the shelf, particularly in the central GoM and areas

immediately surrounding GB. Likewise, the contribution of nanoplankton generally

decreased off-shore in September, with picoplankton becoming more dominant in these waters, coinciding with higher SST and lower [Chl-a] than was observed in April.

A comparison of F_{micro} imagery from the B-NES-SST and MY10 algorithms for April 2019 and September 2019 is shown in Figure 13. Considering the F_{micro} output from the MY10 algorithm is binned to increments of 0.1, the color scale for the B-NES-SST imagery was adjusted to match the scale of the MY10 imagery to facilitate a more visually equitable comparison. The two approaches displayed noticeable similarities and differences. For example, the algorithms showed similarities in the spatial patterns and extent of estimated F_{micro} between the two months, with higher F_{micro} on GB and in the northern GoM than the surrounding region in September, and areas of elevated F_{micro} extending farther off-shore in April. Pixels exceeding the MY10 thresholds of detection (i.e., [Chl-a] > 1.75 mg m^{-3} and $a_{dg}(443) > 0.17$, plotted in white) were located predominantly in shallow regions very close to the coast and within major embayments, with some masked pixels around GB. While the two algorithms showed similar spatial patterns, there were differences in the magnitude of the estimated F_{micro}. For instance, compared with the B-NES-SST model, the MY10-estimated F_{micro} was higher around GB and areas in the GoM and the northern MAB in September, and was also higher within the off-shore feature of elevated [Chl-a] located around 38°N, 69°W in April. The MY10 imagery also displayed a higher degree of spatial variability in F_{micro} compared with that of the B-NES-SST model. This is evident within the central

GoM in April, where the MY10 imagery showed areas of F_{micro} spanning the full fractional range (i.e., 0-1), whereas the B-NES-SST imagery showed a much more uniform distribution of F_{micro}, ranging only between 0.5 and 0.7.
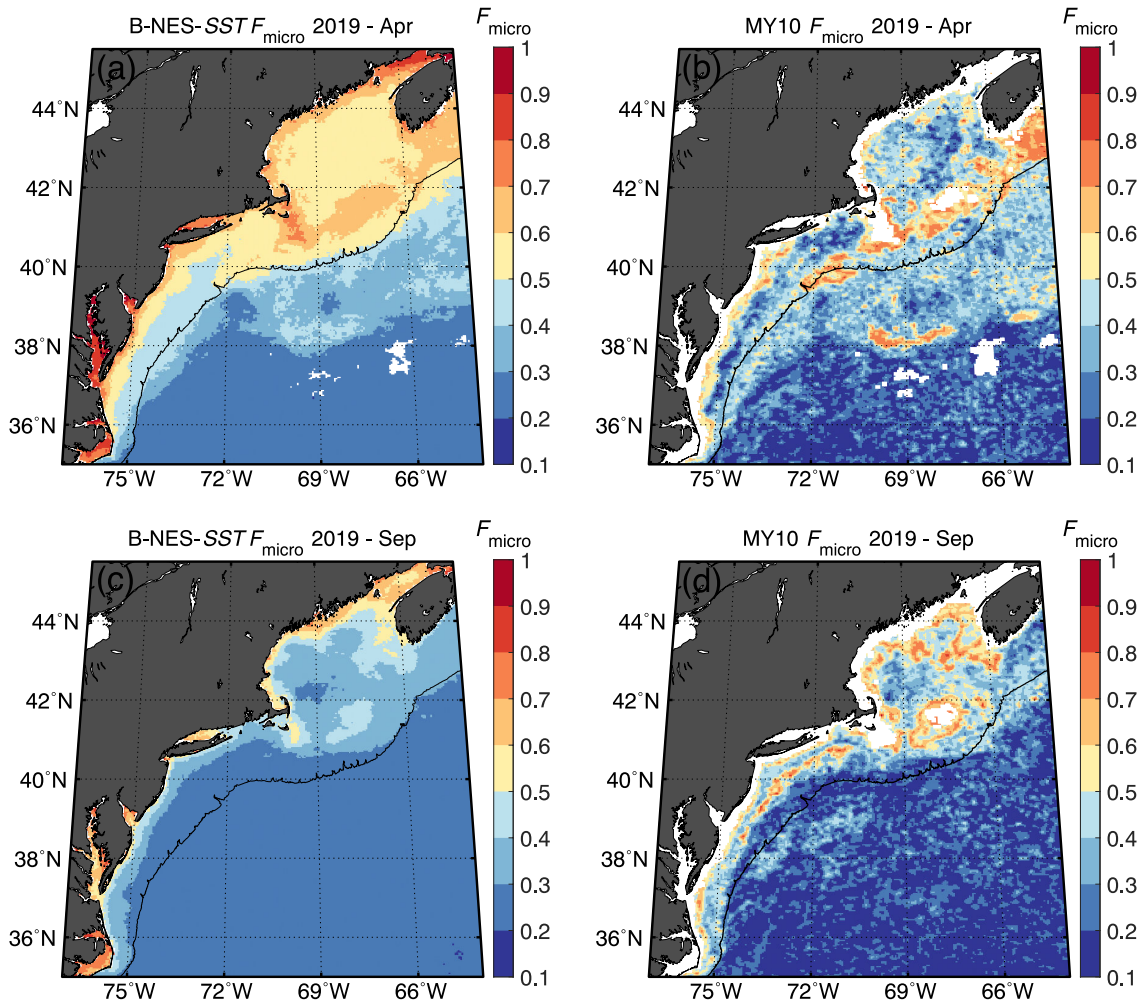
Figure 13. Comparison of monthly F_{micro} imagery from the B-NES-SST and MY10 algorithms for April 2019 (a, b) and September 2019 (c, d). The MY10 algorithm applies a 2-D average filter, masks pixels that exceed defined thresholds of [Chl-a] and a_{dg}(443) (plotted in white), and bins F_{micro} to increments of 0.1 (see Section 2.7.2.2). The color scale for the B-NES-SST imagery was modified to match the output of the MY10 algorithm. The black line indicates the 400 m isobath to mark the approximate location of the shelf break.

4.   DISCUSSION AND CONCLUSIONS

The focus of this study was the regional refinement and evaluation of PSC algorithms in the NES. Like many similar studies, *in situ* estimates of PSCs derived from HPLC pigment data using the DPA method were used for model re-parameterization and statistical comparisons (Uitz et al., 2006; Brewin et al., 2011, 2015a; Hirata et al., 2011; Sun et al., 2018). While this approach is a popular choice given the relative abundance of HPLC samples compared with other methods for quantifying PSCs *in situ*, it has important limitations. First, DPA is not a direct measure of cell size, but rather an approximation of size structure based on assumptions about the taxonomic groups attributed to different pigments, and the size classes represented by those taxa. In reality, pigments are not perfectly diagnostic, and are known to be shared across multiple taxa in varying concentrations dependent on physiological state (Uitz et al., 2008). Further, taxonomic groups may span multiple size classes in ways that are not fully represented by the DPA equations (Leblanc et al., 2018; Nunes et al., 2019). Although proposed modifications to account for some of these biases were incorporated in this study (Devred et al., 2011), the efficacy of this specific approach for characterizing PSCs in the NES region is uncertain and warrants further investigation. Recently, Chase et al., (2020) evaluated the DPA method by comparing pigment-based PSC estimates to coincident measurements of cell size by imaging-in-flow and conventional flow cytometry in the North Atlantic and found that DPA overestimated micro- and picoplankton and underestimated

nanoplankton relative to cytometry. They recommended a revised set of DPA equations to better account for the presence of dinoflagellates and diatoms in the nanoplankton, and the presence of [*TChl-b*] in both pico- and nanoplankton. To reduce uncertainty on this front, continued efforts to inter-compare multiple *in situ* PSC methods across different oceanic environments will be extremely valuable.

Abundance-based PSC algorithms are attractive for their ease of implementation, using satellite [*Chl-a*] as the sole input parameter, and have been shown to perform well globally (Brewin et al., 2011, 2015a) and in a variety of oceanic regions (Brito et al., 2015; Di Cicco et al., 2017; Sun et al., 2018; Gittings et al., 2019). Here, the impact of model re-parameterization was tested using a region-specific HPLC pigment data set, as well as the incorporation of remotely sensed *SST* on the performance of abundance-based PSC models in the NES. The results indicated that regional re-parameterization alone offered minimal statistical improvement relative to other abundance-based models evaluated, which included both globally and regionally parameterized models. Of the eight different models tested, all performed with similar errors and correlation coefficients, particularly for the micro- and combined pico- and nanoplankton classes, when applied to the *in situ* [*Chl-a*] and compared with the pigment-based size class estimates from the independent *in situ* validation data set. There was slightly more variation in the statistical metrics for nano- and picoplankton, but in no instance were the re-parameterized models exclusively the best performing, except for perhaps the H-NES model for estimating picoplankton, which showed

slightly better performance than the other models when applied to both the *in situ* and satellite data.

While re-parameterization alone provided little benefit in terms of improving abundance-based model performance in the NES, the incorporation of remotely sensed *SST* into the re-parameterization of the B10 model did serve to improve PSC prediction accuracy. When applied to the *in situ* validation data set, the regional *SST*-dependent B-NES-*SST* model exhibited a reduction in model error of 10-12% for all size fractions with respect to the *SST*-independent B-NES model. The B-NES-*SST* model also outperformed the other two *SST*-dependent models (B17-*SST* and MB20-*SST*) for all size classes. This result supports what has been shown by previous studies (Ward, 2015; Brewin et al., 2017; Sun et al., 2019; Moore and Brown, 2020) that the addition of *SST* into abundance-based model frameworks can improve PSC prediction accuracy. The relationships between [*Chl-a*], *SST*, and phytoplankton size structure observed in this study were also in general agreement with the findings of these studies, with lower *SST* associated with an increase in the fraction of microplankton and a decrease in the fraction of smaller cells (i.e. pico- and nanoplankton) at similar [*Chl-a*]. This relationship is not surprising, given long-established connections between temperature, water-column stability, nutrient availability, and phytoplankton community size structure in the marine environment (Margalef, 1978; Bouman et al., 2003). While *SST* is used as the additional predictor variable in these models, the associated changes in size structure are not necessarily in direct response to changes in *SST* but rather

the result of a combination of co-varying environmental conditions, including light availability, stratification, and nutrient availability.

Absorption-based algorithms are advantageous over abundance-based methods in that they are rooted in a direct spectral response to phytoplankton cell size, as opposed to relying on indirect statistical connections between [*Chl-a*] and phytoplankton size structure. This means that they can distinguish changes in PSCs that occur outside of the general biomass-size co-variation relationship and are less prone to change over time or geographically. When directly applied to the satellite data, the two absorption-based algorithms examined in this study, C02 and MY10, performed with comparable accuracy to the regionalized abundance-based models. The MY10 algorithm in particular showed statistically similar performance to the *SST*-dependent model, without including any additional environmental information. Considering that pigment-based size class estimates from DPA were used for validation, the similarity in performance for the absorption-based algorithms is encouraging, given they were not developed or parameterized based on the same approach, as was the case with the abundance-based models. This suggests some degree of consistency between estimates of size classes derived from spectral phytoplankton absorption and those determined from HPLC pigment analysis in the NES, as has been previously reported in other regions (Devred et al., 2011).

The PSC algorithms and products evaluated in this study may be useful for validation of or assimilation into regional ecosystem or biogeochemical models

(IOCCG, 2020). However, given the uncertainties associated with the pigment-based size class estimates used for algorithm assessment, as well as the different inputs and outputs between methods, it is difficult to make a definitive determination of which approach is the best choice for such applications. The most suitable method may be dependent on the specifics of the intended application or the questions to be addressed. For instance, biogeochemical models that produce chlorophyll-based phytoplankton size estimates may prefer to compare to abundance-based algorithm outputs, while models that include optics may prefer to compare to output from absorption-based methods – each enabling a more direct comparison dependent on the underlying algorithm/model frameworks and outputs being compared.

In the near future, satellite ocean color remote sensing is moving toward more advanced radiometric instruments with hyperspectral capability and enhanced spatial and temporal resolution (Cetinić et al., 2018). The increased spectral information afforded by these upcoming sensors is anticipated to greatly improve our ability to accurately separate the absorption attributed to different optically significant in-water constituents (i.e., CDOM, NAP, phytoplankton) and retrieve information on phytoplankton community composition and size structure. This improved capability will be particularly relevant to optically complex waters, including coastal and continental shelf regions like the NES ecosystem. Thus, existing absorption-based PSC models may potentially become more robust, and newer methods that exploit the full range of available spectral information will

continue to be developed. Further, to the extent that satellite [*Chl-a*] estimates improve as a result of the increase in spectral resolution, abundance-based approaches may continue to be an effective option for estimating PSCs, especially when combined with *SST* or other ecologically relevant environmental parameters. While not considered in this work, the integration of high-resolution spectral information with environmental data readily attainable from remote sensing should be considered in future PSC algorithm development efforts.

REFERENCES

Bailey, S. W., and Werdell, P. J. (2006). A multi-sensor approach for the on-orbit validation of ocean color satellite data products. *Remote Sens. Environ.* 102, 12–23. doi:10.1016/j.rse.2006.01.015.

Behrenfeld, M. J., O'Malley, R. T., Siegel, D. A., McClain, C. R., Sarmiento, J. L., Feldman, G. C., et al. (2006). Climate-driven trends in contemporary ocean productivity. *Nat. Lond.* 444, 752–5. doi:http://dx.doi.org.uri.idm.oclc.org/10.1038/nature05317.

Boss., E., Claustre, H. (2009). Tara_Oceans_expedition. SeaWiFS Bio-optical Archive and Storage System (SeaBASS), NASA. Accessed: 25 February 2019.http://dx.doi.org/10.5067/SeaBASS/TARA_OCEANS_EXPEDITION/DATA001

Bouman, H. A., Platt, T., Sathyendranath, S., Li, W. K. W., Stuart, V., Fuentes-Yaco, C., et al. (2003). Temperature as indicator of optical properties and community structure of marine phytoplankton:: implications for remote sensing. *Mar. Ecol. Prog. Ser.* 258, 19–30.

Boyce, D. G., Frank, K. T., and Leggett, W. C. (2015). From mice to elephants: overturning the 'one size fits all' paradigm in marine plankton food chains. *Ecol. Lett.* 18, 504–515. doi:10.1111/ele.12434.

Brewin, R. J. W., Brewin, R. J. W., Morán, X. A. G., Raitsos, D. E., Raitsos, D. E., Gittings, J. A., et al. (2019). Factors Regulating the Relationship Between Total and Size-Fractionated Chlorophyll-a in Coastal Waters of the Red Sea. *Front. Microbiol.* 10. doi:10.3389/fmicb.2019.01964.

Brewin, R. J. W., Ciavatta, S., Sathyendranath, S., Jackson, T., Tilstone, G., Curran, K., et al. (2017). Uncertainty in Ocean-Color Estimates of Chlorophyll for Phytoplankton Groups. *Front. Mar. Sci.* 4. doi:10.3389/fmars.2017.00104.

Brewin, R. J. W., Hardman-Mountford, N. J., Lavender, S. J., Raitsos, D. E., Hirata, T., Uitz, J., et al. (2011). An intercomparison of bio-optical techniques for detecting dominant phytoplankton size class from satellite remote sensing. *Remote Sens. Environ.* 115, 325–339. doi:10.1016/j.rse.2010.09.004.

Brewin, R. J. W., Hirata, T., Hardman-Mountford, N. J., Lavender, S. J., Sathyendranath, S., and Barlow, R. (2012). The influence of the Indian Ocean Dipole on interannual variations in phytoplankton size structure as revealed by Earth Observation. *Deep Sea Res. Part II Top. Stud. Oceanogr.* 77–80, 117–127. doi:10.1016/j.dsr2.2012.04.009.

Brewin, R. J. W., Sathyendranath, S., Hirata, T., Lavender, S. J., Barciela, R. M., and Hardman-Mountford, N. J. (2010). A three-component model of phytoplankton size class for the Atlantic Ocean. *Ecol. Model.* 221, 1472–1483. doi:10.1016/j.ecolmodel.2010.02.014.

Brewin, R. J. W., Sathyendranath, S., Jackson, T., Barlow, R., Brotas, V., Airs, R., et al. (2015a). Influence of light in the mixed-layer on the parameters of a three-component model of phytoplankton size class. *Remote Sens. Environ.* 168, 437–450. doi:10.1016/j.rse.2015.07.004.

Brewin, R. J. W., Sathyendranath, S., Müller, D., Brockmann, C., Deschamps, P.-Y., Devred, E., et al. (2015b). The Ocean Colour Climate Change Initiative: III. A round-robin comparison on in-water bio-optical algorithms. *Remote Sens. Environ.* 162, 271–294. doi:10.1016/j.rse.2013.09.016.

Bricaud, A. (2004). Natural variability of phytoplanktonic absorption in oceanic waters: Influence of the size structure of algal populations. *J. Geophys. Res.* 109. doi:10.1029/2004JC002419.

Bricaud, A., Bédhomme, A.-L., and Morel, A. (1988). Optical properties of diverse phytoplanktonic species: experimental results and theoretical interpretation. *J. Plankton Res.* 10, 851–873. doi:10.1093/plankt/10.5.851.

Brito, A. C., Sá, C., Brotas, V., Brewin, R. J. W., Silva, T., Vitorino, J., et al. (2015). Effect of phytoplankton size classes on bio-optical properties of phytoplankton in the Western Iberian coast: Application of models. *Remote Sens. Environ.* 156, 537–550. doi:10.1016/j.rse.2014.10.020.

Caron, D. A., Countway, P. D., Jones, A. C., Kim, D. Y., and Schnetzer, A. (2012). Marine Protistan Diversity. *Annu. Rev. Mar. Sci.* 4, 467–493. doi:10.1146/annurev-marine-120709-142802.

Cetinić, I., McClain, C. R., and Werdell, P. J. (2018). PACE Technical Report Series. 2, 316.

Chase, A. P., Kramer, S. J., Haëntjens, N., Boss, E. S., Karp-Boss, L., Edmondson, M., et al. (2020). Evaluation of diagnostic pigments to estimate phytoplankton size classes. *Limnol. Oceanogr. Methods* n/a. doi:10.1002/lom3.10385.

Chekalyuk, A. (2008). Del_Ches_Bay_Fluorescence. SeaWiFS Bio-optical Archive and Storage System (SeaBASS), NASA. Accessed: 25 February 2019. http://dx.doi.org/10.5067/SeaBASS/DEL_CHES_BAY_FLUORESCENCE/DATA001

Chin, T. M., Vazquez-Cuervo, J., and Armstrong, E. M. (2017). A multi-scale high-resolution analysis of global sea surface temperature. *Remote Sens. Environ.* 200, 154–169. doi:10.1016/j.rse.2017.07.029.

Chisholm, S. W., Olson, R. J., Zettler, E. R., Goericke, R., Waterbury, J. B., and Welschmeyer, N. A. (1988). A novel free-living prochlorophyte abundant in the oceanic euphotic zone. *Nature* 334, 340–343. doi:10.1038/334340a0.

Ciotti, A. M., and Bricaud, A. (2006). Retrievals of a size parameter for phytoplankton and spectral light absorption by colored detrital matter from water-leaving radiances at SeaWiFS channels in a continental shelf region off Brazil: Algal size and CDM from SeaWiFS data. *Limnol. Oceanogr. Methods* 4, 237–253. doi:10.4319/lom.2006.4.237.

Ciotti, Á. M., Lewis, M. R., and Cullen, J. J. (2002). Assessment of the relationships between dominant cell size in natural phytoplankton communities and the spectral shape of the absorption coefficient. *Limnol. Oceanogr.* 47, 404–417. doi:10.4319/lo.2002.47.2.0404.

Claustre, H. (2005). Toward a taxon-specific parameterization of bio-optical models of primary production: A case study in the North Atlantic. *J. Geophys. Res.* 110. doi:10.1029/2004JC002634.

Devred, E., Sathyendranath, S., Stuart, V., Maass, H., Ulloa, O., and Platt, T. (2006). A two-component model of phytoplankton absorption in the open ocean: Theory and applications. *J. Geophys. Res. Oceans* 111. doi:10.1029/2005JC002880.

Devred, E., Sathyendranath, S., Stuart, V., and Platt, T. (2011). A three component classification of phytoplankton absorption spectra: Application to ocean-color data. *Remote Sens. Environ.* 115, 2255–2266. doi:10.1016/j.rse.2011.04.025.

Di Cicco, A., Sammartino, M., Marullo, S., and Santoleri, R. (2017). Regional Empirical Algorithms for an Improved Identification of Phytoplankton Functional Types and Size Classes in the Mediterranean Sea Using Satellite Data. *Front. Mar. Sci.* 4. doi:10.3389/fmars.2017.00126.

Dierssen, H. M. (2010). Perspectives on empirical approaches for ocean color remote sensing of chlorophyll in a changing climate. *Proc. Natl. Acad. Sci.* 107, 17073–17078. doi:10.1073/pnas.0913800107.

Efron, B. (1979). Bootstrap Methods: Another Look at the Jackknife. *Ann. Stat.* 7, 1–26. doi:10.1214/aos/1176344552.

Field, C. B., Behrenfeld, M. J., Randerson, J. T., and Falkowski, P. (1998). Primary Production of the Biosphere: Integrating Terrestrial and Oceanic Components. *Science* 281, 237–240.

Finkel, Z. V., Beardall, J., Flynn, K. J., Quigg, A., Rees, T. A. V., and Raven, J. A. (2010). Phytoplankton in a changing world: cell size and elemental stoichiometry. *J. Plankton Res.* 32, 119–137. doi:10.1093/plankt/fbp098.

Friedland, K. D., Record, N. R., Asch, R. G., Kristiansen, T., Saba, V. S., Drinkwater, K. F., et al. (2016). Seasonal phytoplankton blooms in the North Atlantic linked to the overwintering strategies of copepods. *Elem Sci Anth* 4, 000099. doi:10.12952/journal.elementa.000099.

Gittings, J. A., Brewin, R. J. W., Raitsos, D. E., Kheireddine, M., Ouhssain, M., Jones, B. H., et al. (2019). Remotely sensing phytoplankton size structure in the Red Sea. *Remote Sens. Environ.* 234, 111387. doi:10.1016/j.rse.2019.111387.

Gohin, F., Druon, J. N., and Lampert, L. (2002). A five channel chlorophyll concentration algorithm applied to SeaWiFS data processed by SeaDAS in coastal waters. *Int. J. Remote Sens.* 23, 1639–1661. doi:10.1080/01431160110071879.

Gould, R. (2009). 2009oct_Chesapeake. SeaWiFS Bio-optical Archive and Storage System (SeaBASS), NASA. Accessed: 25 February 2019. http://dx.doi.org/10.5067/SeaBASS/2009OCT_CHESAPEAKE/DATA001

Grunert, B. K., Mouw, C. B., and Ciochetto, A. B. (2019). Deriving inherent optical properties from decomposition of hyperspectral non-water absorption. *Remote Sens. Environ.* 225, 193–206. doi:10.1016/j.rse.2019.03.004.

Guidi, L., Stemmann, L., Jackson, G. A., Ibanez, F., Claustre, H., Legendre, L., et al. (2009). Effects of phytoplankton community on production, size, and export of large aggregates: A world-ocean analysis. *Limnol. Oceanogr.* 54, 1951–1963. doi:10.4319/lo.2009.54.6.1951.

Harding, L., Mallonee, M. (2001). BIOCOMPLEXITY. SeaWiFS Bio-optical Archive and Storage System (SeaBASS), NASA. Accessed: 25 February 2019. http://dx.doi.org/10.5067/SeaBASS/BIOCOMPLEXITY/DATA001

Hare, J. A., Morrison, W. E., Nelson, M. W., Stachura, M. M., Teeters, E. J., Griffis, R. B., et al. (2016). A Vulnerability Assessment of Fish and Invertebrates to Climate Change on the Northeast U.S. Continental Shelf. *PLOS ONE* 11, e0146756. doi:10.1371/journal.pone.0146756.

Hirata, T., Hardman-Mountford, N. J., Brewin, R. J. W., Aiken, J., Barlow, R., Suzuki, K., et al. (2011). Synoptic relationships between surface Chlorophyll-*a* and diagnostic pigments specific to phytoplankton functional types. *Biogeosciences* 8, 311–327. doi:10.5194/bg-8-311-2011.

Hooker, S. (2000). COASTAL. SeaWiFS Bio-optical Archive and Storage System (SeaBASS), NASA. Accessed: 25 February 2019. http://dx.doi.org/10.5067/SeaBASS/COASTAL/DATA001

Hooker, S., Lee, Z., Mannino, A., Twardowski, M., Voss, K. (2007). Ocean_Color_Cal_Val. SeaWiFS Bio-optical Archive and Storage System (SeaBASS), NASA. Accessed: 25 February 2019. http://dx.doi.org/10.5067/SeaBASS/OCEAN_COLOR_CAL_VAL/DATA00 1

Hu, C., Lee, Z., and Franz, B. (2012). Chlorophyll aalgorithms for oligotrophic oceans: A novel approach based on three-band reflectance difference. *J. Geophys. Res. Oceans* 117. doi:10.1029/2011JC007395.

Hunter-Cevera, K. R., Neubert, M. G., Olson, R. J., Solow, A. R., Shalapyonok, A., and Sosik, H. M. (2016). Physiological and ecological drivers of early spring blooms of a coastal phytoplankter. *Science* 354, 326–329. doi:10.1126/science.aaf8536.

IOCCG (2014). Phytoplankton Functional Types from Space. Sathyendranath, S. (ed.), Reports of the International Ocean-Colour Coordinating Group, No. 15. Dartmouth, Canada.: IOCCG Available at: https://ioccg.org/wp-content/uploads/2018/09/ioccg_report_15_2014.pdf [Accessed November 21, 2019].

IOCCG (2020). Synergy between Ocean Colour and Biogeochemical/ Ecosystem Models. Dartmouth, Canada.: IOCCG Available at: https://ioccg.org/wp-content/uploads/2020/01/ioccg_report_modelling-vol-19-rr.pdf [Accessed November 10, 2020].

Jackson, T., Sathyendranath, S., and Mélin, F. (2017). An improved optical classification scheme for the Ocean Colour Essential Climate Variable and its applications. *Remote Sens. Environ.* 203, 152–161. doi:10.1016/j.rse.2017.03.036.

Kleisner, K. M., Fogarty, M. J., McGee, S., Hare, J. A., Moret, S., Perretti, C. T., et al. (2017). Marine species distribution shifts on the U.S. Northeast Continental Shelf under continued ocean warming. *Prog. Oceanogr.* 153, 24–36. doi:10.1016/j.pocean.2017.04.001.

Kostadinov, T. S., Cabré, A., Vedantham, H., Marinov, I., Bracher, A., Brewin, R. J. W., et al. (2017). Inter-comparison of phytoplankton functional type phenology metrics derived from ocean color algorithms and Earth System Models. *Remote Sens. Environ.* 190, 162–177. doi:10.1016/j.rse.2016.11.014.

Lamont, T., Brewin, R. J. W., and Barlow, R. G. (2018). Seasonal variation in remotely-sensed phytoplankton size structure around southern Africa. *Remote Sens. Environ.* 204, 617–631. doi:10.1016/j.rse.2017.09.038.

Laws, E. A., and Archie, J. W. (1981). Appropriate use of regression analysis in marine biology. *Mar. Biol.* 65, 13–16. doi:10.1007/BF00397062.

Leblanc, K., Quéguiner, B., Diaz, F., Cornet, V., Michel-Rodriguez, M., Durrieu de Madron, X., et al. (2018). Nanoplanktonic diatoms are globally overlooked but play a role in spring blooms and carbon export. *Nat. Commun.* 9, 953. doi:10.1038/s41467-018-03376-9.

Lee, Z., Carder, K. L., and Arnone, R. A. (2002). Deriving inherent optical properties from water color: a multiband quasi-analytical algorithm for optically deep waters. *Appl. Opt.* 41, 5755–5772. doi:10.1364/AO.41.005755.

Lee, Z., Lubac, B., Werdell, J., and Arnone, R. (2009). An Update of the Quasi-Analytical Algorithm (QAA_v5). International Ocean Colour Coordinating Group (IOCCG) Available at: https://ioccg.org/groups/Software_OCA/QAA_v5.pdf [Accessed April 29, 2020].

Liu, X., Devred, E., and Johnson, C. (2018). Remote Sensing of Phytoplankton Size Class in Northwest Atlantic from 1998 to 2016: Bio-Optical Algorithms Comparison and Application. *Remote Sens.* 10, 1028. doi:10.3390/rs10071028.

Longhurst, A., Sathyendranath, S., Platt, T., and Caverhill, C. (1995). An estimate of global primary production in the ocean from satellite radiometer data. *J. Plankton Res.* 17, 1245–1271. doi:10.1093/plankt/17.6.1245.

Mackey, M., Mackey, D., Higgins, H., and Wright, S. (1996). CHEMTAX - a program for estimating class abundances from chemical markers:application to HPLC measurements of phytoplankton. *Mar. Ecol. Prog. Ser.* 144, 265–283. doi:10.3354/meps144265.

Mannino, A., Mulholland, M., Hyde, K. (2009). CliVEC. SeaWiFS Bio-optical Archive and Storage System (SeaBASS), NASA. Accessed: 25 February 2019. http://dx.doi.org/10.5067/SeaBASS/CLIVEC/DATA001

Mannino, A., Novak, M. G., Hooker, S. B., Hyde, K., and Aurin, D. (2014). Algorithm development and validation of CDOM properties for estuarine and continental shelf waters along the northeastern U.S. coast. *Remote Sens. Environ.* 152, 576–602. doi:10.1016/j.rse.2014.06.027.

Mannino, A., Ondrusek, M. (2013). ECOMON. SeaWiFS Bio-optical Archive and Storage System (SeaBASS), NASA. Accessed: 25 February 2019. http://dx.doi.org/10.5067/SeaBASS/ECOMON/DATA001

Mannino, A., Ondrusek, M., Salisbury, J. (2015). ECOA. SeaWiFS Bio-optical Archive and Storage System (SeaBASS), NASA. Accessed: 25 February 2019. http://dx.doi.org/10.5067/SeaBASS/ECOA/DATA001

Marañón, E. (2015). Cell Size as a Key Determinant of Phytoplankton Metabolism and Community Structure. *Annu. Rev. Mar. Sci.* 7, 241–264. doi:10.1146/annurev-marine-010814-015955.

Margalef, R. (1978). Life-forms of phytoplankton as survival alternatives in an unstable environment. *Oceanol. Acta.* doi:null.

Marinov, I., Doney, S. C., and Lima, I. D. (2010). Response of ocean phytoplankton community structure to climate change over the 21st century: partitioning the effects of nutrients, temperature and light. *Biogeosciences* 7, 3941–3959. doi:10.5194/bg-7-3941-2010.

Marra, J. (2008). ONDEQUE. SeaWiFS Bio-optical Archive and Storage System (SeaBASS), NASA. Accessed: 25 February 2019. http://dx.doi.org/10.5067/SeaBASS/ONDEQUE/DATA001

Mobley, C. D., and Sundman, L. K. (2013). HYDROLIGHT 5.2 ECOLIGHT 5.2 Technical Documentation. Available at: https://www.sequoiasci.com/wp-content/uploads/2013/07/HE52TechDoc.pdf [Accessed October 26, 2020].

Moore, T. (2006). Western_Gulf_of_Maine. SeaWiFS Bio-optical Archive and Storage System (SeaBASS), NASA. Accessed: 25 February 2019. http://dx.doi.org/10.5067/SeaBASS/WESTERN_GULF_OF_MAINE/DATA001

Moore, T. S., and Brown, C. W. (2020). Incorporating environmental data in abundance-based algorithms for deriving phytoplankton size classes in the Atlantic Ocean. *Remote Sens. Environ.* 240, 111689. doi:10.1016/j.rse.2020.111689.

Moore, T. S., Campbell, J. W., and Dowell, M. D. (2009). A class-based approach to characterizing and mapping the uncertainty of the MODIS ocean

chlorophyll product. *Remote Sens. Environ.* 113, 2424–2430. doi:10.1016/j.rse.2009.07.016.

Morán, X. A. G., López-Urrutia, Á., Calvo-Díaz, A., and Li, W. K. W. (2010). Increasing importance of small phytoplankton in a warmer ocean. *Glob. Change Biol.* 16, 1137–1144. doi:10.1111/j.1365-2486.2009.01960.x.

Morel, A. (1987). Chlorophyll-specific scattering coefficient of phytoplankton. A simplified theoretical approach. *Deep Sea Res. Part Oceanogr. Res. Pap.* 34, 1093–1105. doi:10.1016/0198-0149(87)90066-5.

Morel, A., and Bricaud, A. (1981). Theoretical results concerning light absorption in a discrete medium, and application to specific absorption of phytoplankton. *Deep Sea Res. Part Oceanogr. Res. Pap.* 28, 1375–1393. doi:10.1016/0198-0149(81)90039-X.

Mouw, C. B., Barnett, A., McKinley, G. A., Gloege, L., and Pilcher, D. (2016). Phytoplankton size impact on export flux in the global ocean. *Glob. Biogeochem. Cycles* 30, 1542–1562. doi:10.1002/2015GB005355.

Mouw, C. B., Ciochetto, A. B., Grunert, B., and Yu, A. (2017a). Expanding understanding of optical variability in Lake Superior with a 4-year dataset. *Earth Syst. Sci. Data* 9, 497–509. doi:10.5194/essd-9-497-2017.

Mouw, C. B., Hardman-Mountford, N. J., Alvain, S., Bracher, A., Brewin, R. J. W., Bricaud, A., et al. (2017b). A Consumer's Guide to Satellite Remote Sensing of Multiple Phytoplankton Groups in the Global Ocean. *Front. Mar. Sci.* 4. doi:10.3389/fmars.2017.00041.

Mouw, C. B., and Yoder, J. A. (2010). Optical determination of phytoplankton size composition from global SeaWiFS imagery. *J. Geophys. Res.* 115. doi:10.1029/2010JC006337.

Mouw, C. B., Yoder, J. A., and Doney, S. C. (2012). Impact of phytoplankton community size on a linked global ocean optical and ecosystem model. *J. Mar. Syst.* 89, 61–75. doi:10.1016/j.jmarsys.2011.08.002.

Mueller, J. L., Fargion, G. S., and McClain, C. R. (2003). Ocean Optics Protocols for Satellite Ocean Color Sensor Validation. Greenbelt, MD, USA: NASA Available at: https://oceancolor.gsfc.nasa.gov/docs/technical/protocols_ver4_voliv.pdf [Accessed October 19, 2020].

Nair, A., Sathyendranath, S., Platt, T., Morales, J., Stuart, V., Forget, M.-H., et al. (2008). Remote sensing of phytoplankton functional types. *Remote Sens. Environ.* 112, 3366–3375. doi:10.1016/j.rse.2008.01.021.

National Marine Fisheries Service (2018). Fisheries Economics of the United States 2016. U.S. Department of Commerce.

National Marine Fisheries Service (2020). Cruise Results: NOAA Research Vessel GORDON GUNTER, Cruise No. GU 19-05, Fall Northeast Ecosystem Monitoring Survey. doi:10.25923/ah4q-2b94.

Nunes, S., Perez, G. L., Latasa, M., Zamanillo, M., Delgado, M., Ortega-Retuerta, E., et al. (2019). Size fractionation, chemotaxonomic groups and bio-optical properties of phytoplankton along a transect from the Mediterranean Sea to the SW Atlantic Ocean. *Sci. Mar.* 83, 87. doi:10.3989/scimar.04866.10A.

Olson, R. J., and Sosik, H. M. (2007). A submersible imaging-in-flow instrument to analyze nano-and microplankton: Imaging FlowCytobot. *Limnol. Oceanogr. Methods* 5, 195–203. doi:10.4319/lom.2007.5.195.

O'Reilly, J. E., Maritorena, S., Mitchell, B. G., Siegel, D. A., Carder, K. L., Garver, S. A., et al. (1998). Ocean color chlorophyll algorithms for SeaWiFS. *J. Geophys. Res. Oceans* 103, 24937–24953. doi:10.1029/98JC02160.

O'Reilly, J. E., and Zetlin, C. (1998). Seasonal, Horizonal, and Vertical Distribution of Phytoplankton Chlorophyll a in the Northeast U.S. Continental Shelf Ecosystem. NOAA National Marine Fisheries Service.

Pan, X., Mannino, A., Marshall, H. G., Filippino, K. C., and Mulholland, M. R. (2011). Remote sensing of phytoplankton community composition along the northeast coast of the United States. *Remote Sens. Environ.* 115, 3731–3747. doi:10.1016/j.rse.2011.09.011.

Pan, X., Mannino, A., Russ, M. E., and Hooker, S. B. (2008). Remote sensing of the absorption coefficients and chlorophyll a concentration in the United States southern Middle Atlantic Bight from SeaWiFS and MODIS-Aqua. *J. Geophys. Res. Oceans* 113. doi:10.1029/2008JC004852.

Pan, X., Mannino, A., Russ, M. E., Hooker, S. B., and Harding, L. W. (2010). Remote sensing of phytoplankton pigment distribution in the United States northeast coast. *Remote Sens. Environ.* 114, 2403–2416. doi:10.1016/j.rse.2010.05.015.

Pershing, A. J., Alexander, M. A., Hernandez, C. M., Kerr, L. A., Bris, A. L., Mills, K. E., et al. (2015). Slow adaptation in the face of rapid warming leads to collapse of the Gulf of Maine cod fishery. *Science* 350, 809–812. doi:10.1126/science.aac9819.

Platt, T., and Sathyendranath, S. (2008). Ecological indicators for the pelagic zone of the ocean from remote sensing. *Remote Sens. Environ.* 112, 3426–3436. doi:10.1016/j.rse.2007.10.016.

Quéré, C. L., Harrison, S. P., Prentice, I. C., Buitenhuis, E. T., Aumont, O., Bopp, L., et al. (2005). Ecosystem dynamics based on plankton functional types for global ocean biogeochemistry models. *Glob. Change Biol.* 11, 2016–2040. doi:10.1111/j.1365-2486.2005.1004.x.

Raven, J. A. (1998). The twelfth Tansley Lecture. Small is beautiful: the picophytoplankton. *Funct. Ecol.* 12, 503–513. doi:10.1046/j.1365-2435.1998.00233.x.

Richaud, B., Kwon, Y.-O., Joyce, T. M., Fratantoni, P. S., and Lentz, S. J. (2016). Surface and bottom temperature and salinity climatology along the continental shelf off the Canadian and U.S. East Coasts. *Cont. Shelf Res.* 124, 165–181. doi:10.1016/j.csr.2016.06.005.

Roesler, C. (2009). LOBO_timeseries. SeaWiFS Bio-optical Archive and Storage System (SeaBASS), NASA. Accessed: 25 February 2019. http://dx.doi.org/10.5067/SeaBASS/LOBO_TIMESERIES/DATA001

Roy, S. (2011). *Phytoplankton Pigments : Characterization, Chemotaxonomy and Applications in Oceanography*. Cambridge: Cambridge University Press Available at: http://uri.idm.oclc.org/login?url=http://search.ebscohost.com/login.aspx?direct=true&db=e000xna&AN=409037&site=ehost-live&scope=site.

Saba, V. S., Hyde, K. J. W., Rebuck, N. D., Friedland, K. D., Hare, J. A., Kahru, M., et al. (2015). Physical associations to spring phytoplankton biomass interannual variability in the U.S. Northeast Continental Shelf. *J. Geophys. Res. Biogeosciences* 120, 205–220. doi:10.1002/2014JG002770.

Sathyendranath, S., Brewin, R. J. W., Brockmann, C., Brotas, V., Calton, B., Chuprin, A., et al. (2019). An Ocean-Colour Time Series for Use in Climate Studies: The Experience of the Ocean-Colour Climate Change Initiative (OC-CCI). *Sensors* 19, 4285. doi:10.3390/s19194285.

Sathyendranath, S., Cota, G., Stuart, V., Maass, H., and Platt, T. (2001). Remote sensing of phytoplankton pigments: A comparison of empirical and theoretical approaches. *Int. J. Remote Sens.* 22, 249–273. doi:10.1080/014311601449925.

Sauer, M. J., Roesler, C. S., Werdell, P. J., and Barnard, A. (2012). Under the hood of satellite empirical chlorophyll a algorithms: revealing the dependencies

of maximum band ratio algorithms on inherent optical properties. *Opt. Express* 20, 20920. doi:10.1364/OE.20.020920.

Schollaert, S. E., Rossby, T., and Yoder, J. A. (2004). Gulf Stream cross-frontal exchange: possible mechanisms to explain interannual variations in phytoplankton chlorophyll in the Slope Sea during the SeaWiFS years. *Deep Sea Res. Part II Top. Stud. Oceanogr.* 51, 173–188. doi:10.1016/j.dsr2.2003.07.017.

Seegers, B. N., Stumpf, R. P., Schaeffer, B. A., Loftin, K. A., and Werdell, P. J. (2018). Performance metrics for the assessment of satellite data products: an ocean color case study. *Opt. Express* 26, 7404–7422.

Sieburth, J. McN., Smetacek, V., and Lenz, J. (1978). Pelagic ecosystem structure: Heterotrophic compartments of the plankton and their relationship to plankton size fractions 1. *Limnol. Oceanogr.* 23, 1256–1263. doi:10.4319/lo.1978.23.6.1256.

Sun, X., Shen, F., Brewin, R. J. W., Liu, D., and Tang, R. (2019). Twenty-Year Variations in Satellite-Derived Chlorophyll-a and Phytoplankton Size in the Bohai Sea and Yellow Sea. *J. Geophys. Res. Oceans* 124, 8887–8912. doi:10.1029/2019JC015552.

Sun, X., Shen, F., Liu, D., Bellerby, R. G. J., Liu, Y., and Tang, R. (2018). In Situ and Satellite Observations of Phytoplankton Size Classes in the Entire Continental Shelf Sea, China. *J. Geophys. Res. Oceans* 123, 3523–3544. doi:10.1029/2017JC013651.

Torrecilla, E., Stramski, D., Reynolds, R. A., Millán-Núñez, E., and Piera, J. (2011). Cluster analysis of hyperspectral optical data for discriminating phytoplankton pigment assemblages in the open ocean. *Remote Sens. Environ.* 115, 2578–2593. doi:10.1016/j.rse.2011.05.014.

Uitz, J., Claustre, H., Morel, A., and Hooker, S. B. (2006). Vertical distribution of phytoplankton communities in open ocean: An assessment based on surface chlorophyll. *J. Geophys. Res. Oceans* 111. doi:10.1029/2005JC003207.

Uitz, J. U., Huot, Y., Bruyant, F., Babin, M., and Claustre, H. (2008). Relating phytoplankton photophysiological properties to community structure on large scales. *Limnol. Oceanogr.* 53, 614–630. doi:10.4319/lo.2008.53.2.0614.

Vidussi, F., Claustre, H., Manca, B. B., Luchetta, A., and Marty, J.-C. (2001). Phytoplankton pigment distribution in relation to upper thermocline

circulation in the eastern Mediterranean Sea during winter. *J. Geophys. Res. Oceans* 106, 19939–19956. doi:10.1029/1999JC000308.

Ward, B. A. (2015). Temperature-Correlated Changes in Phytoplankton Community Structure Are Restricted to Polar Waters. *PLOS ONE* 10, e0135581. doi:10.1371/journal.pone.0135581.

Werdell, P. J., Franz, B. A., Bailey, S. W., Feldman, G. C., Boss, E., Brando, V. E., et al. (2013). Generalized ocean color inversion model for retrieving marine inherent optical properties. *Appl. Opt.* 52, 2019. doi:10.1364/AO.52.002019.

Willmott, C. J., and Matsuura, K. (2005). Advantages of the mean absolute error (MAE) over the root mean square error (RMSE) in assessing average model performance. *Clim. Res.* 30, 79–82.

Xu, F., and Ignatov, A. (2014). In situ SST Quality Monitor (*i* Quam). *J. Atmospheric Ocean. Technol.* 31, 164–180. doi:10.1175/JTECH-D-13-00121.1.

Yentsch, C. S., and Phinney, D. A. (1989). A bridge between ocean optics and microbial ecology: Ocean optics and microbial ecology. *Limnol. Oceanogr.* 34, 1694–1705. doi:10.4319/lo.1989.34.8.1694.